Role of compaction in melt extraction and accumulation at a slow spreading center: Microstructures of olivine gabbros from the Atlantis Bank (IODP Hole U1473A, SWIR)

Carlotta Ferrando [a, b, *], Valentin Basch [b], Benoit Ildefonse [c], Jeremy Deans [d], Alessio Sanfilippo [b], Fabrice Barou [c], Lydéric France [a]

[a] Université de Lorraine, CNRS, CRPG, Nancy, France
[b] Dipartimento di Scienze della Terra e dell'Ambiente, Università degli Studi di Pavia, Pavia, Italy
[c] Géosciences Montpellier, Université de Montpellier, CNRS, Montpellier, France
[d] School of Biological, Environmental, and Earth Sciences, University of Southern Mississippi, MS, United States

A B S T R A C T

The exposure of gabbroic sequences at Oceanic Core Complexes (OCC) along ultraslow- to slow-spreading ridges permits the study of the processes forming the lower oceanic crust. On top of the Atlantis Bank OCC along the ultraslow-spreading Southwest Indian Ridge, IODP Expedition 360 drilled Hole U1473A, mainly composed of primitive olivine gabbros interspersed with more evolved Ti-Fe oxide-bearing gabbros and minor felsic veins. These rocks record a complex history of protracted magmatism during continuous uplift and deformation of the gabbroic sequence. Extensive crystal-plastic deformation is dominantly recorded in the shallower sections of the drillhole, whereas the deeper sections better preserve primary magmatic features. We focus on microstructures, including intra-crystalline deformation of rock-forming minerals, and plagioclase crystallographic preferred orientations of olivine gabbros lacking evidence for exhumation-related crystal plastic deformation, to gain insights on the relationship between compaction, melt migration and melt accumulation during the early magmatic history of this section of lower oceanic crust. Olivine gabbros are characterized by ubiquitous grain-size variations, from coarse- to fine-grained intervals. Minerals in coarse-grained intervals show intra-crystalline deformation, while fine-grained crystals lack internal strain. Bent coarse-grained plagioclase associated with weak magmatic foliation and lack of lineation suggest that the coarse-grained intervals were deformed under weak compaction. On the other hand, crystallographic preferred orientations of undeformed fine-grained plagioclase show weak lineations, likely indicative of non-coaxial strain. We thereby infer that the coarse-grained intervals underwent ongoing weak compaction from the stage of olivine + plagioclase ± clinopyroxene crystal mush to the melt-poor stage, and that this process likely aided melt extraction and accumulation in discrete melt-rich zones where crystals orientated in the direction of magmatic flow. Crystallization of melts in the melt-rich zones ultimately formed the fine-grained intervals at different depths in Hole U1473A. This indicates that processes of compaction can lead to local chemical and grain-size heterogeneities in a lower crustal section, while had a minor role in the melt movement at larger scales (e.g., the whole crystal mush) within the oceanic crust.

1. Introduction

A thick (2 km) section of magmatic lower oceanic crust is exposed at the Atlantis Bank Oceanic Core Complex (OCC), representing one of the best studied examples of ultraslow-spreading oceanic crust in the world. The vertical structure of the Atlantis Bank gabbroic sequence was interpreted as resulting from multiple melt injections forming ephemeral crystal mush bodies of ~400 m maximum thickness (Natland and Dick, 2001; Natland and Dick, 2002; Dick et al., 2000, 2019a, 2019b; MacLeod et al., 2017; Boulanger et al., 2020) that cooled at relatively rapid rates of ~0.005 °C/yr (John et al., 2004; Coogan et al., 2007).

Single bodies of crystallized crystal mush were identified by upward chemically differentiated units of 200 to 400 m thickness (Dick et al.,

---

* Corresponding author at: Université de Lorraine, CNRS, CRPG, Nancy, France.
  E-mail address: ottaferrando@gmail.com (C. Ferrando).

2000; Natland and Dick, 2002). These chemical trends were defined using bulk-rock (Natland and Dick, 2002) and mineral chemical compositions (mainly Mg# and Cr_2O_3 in clinopyroxene, An contents in plagioclase and Mg# in olivine; Dick et al., 2002; Boulanger et al., 2020; Ferrando et al., 2021; Zhang et al., 2020, 2021) progressively evolving toward the top of each magmatic section. To form these chemical trends, melts must have migrated upward as they progressively differentiated within the crystal mushes. Porous melt migration through the Atlantis Bank lower oceanic crust has been described at all scales. Sanfilippo et al. (2020) described the occurrence of a cm-scale 'compositional band' in an apparently homogeneous sample of Atlantis Bank olivine gabbro. They interpreted this band as a record of cryptic melt migration through a primitive crystal mush. At the scale of a single crystal mush reservoir (~300 m thick), Boulanger et al. (2020) proposed that upward melt mobilization by porous flow facilitated the collection of melts from the deepest portions of a gabbroic mush, composed of stacked sills, to an overlying crystal mush constituting the upper half of the reservoir. Also, considering the reconstructed vertical structure of the Atlantis Bank OCC, the increasing modal abundance of oxide gabbros toward the top of the oceanic crustal sequence further suggests melt migration of progressively evolving intercumulus melts (Dick et al., 2000; Natland and Dick, 2001; Zhang et al., 2020).

Porous melt migration has been invoked as a magmatic process playing a major role in the generation of lower oceanic crusts (e.g., Coogan et al., 2000; Lissenberg et al., 2013, 2019; Leuthold et al., 2014; Sanfilippo et al., 2015; Basch et al., 2018, 2019; Ferrando et al., 2018; Dick et al., 2019a; Boulanger et al., 2020; Rampone et al., 2020; Zhang et al., 2020), and as a process capable to modify melts that possibly contribute to erupted MORBs (Lissenberg and Dick, 2008). In crystal mushes, because the density of the melt is lower than the fractionated crystals, the positive buoyancy of melts can drive their upward migration (McKenzie, 1984; Lissenberg et al., 2019). Melt transport can be also aided by compaction during the early stages (i.e., crystal mush stages) of magma crystallization (e.g., Nicolas, 1992) as commonly inferred in both oceanic (e.g., Natland and Dick, 2001; VanTongeren et al., 2015; Brown et al., 2019; Lissenberg et al., 2019; Zhang et al., 2020) and continental environments (e.g., Meurer and Boudreau, 1998; Namur et al., 2015; Holness et al., 2017; Bertolett et al., 2019). Compaction of crystal piles may result from coaxial strain (Nicolas, 1992), and has been well documented in Layered Mafic Intrusions by the occurrence of bent and interlocked crystals of plagioclase, together with strong plagioclase shape preferred orientation (e.g., Meurer and Boudreau, 1998; Holness et al., 2017; Bertolett et al., 2019).

At slow-spreading ridges, compaction of gabbroic sequences has been invoked as the process driving melt migration and generating the upward chemical trends in single crystal mush bodies (e.g., Natland and Dick, 2001; Lissenberg et al., 2019; Zhang et al., 2020). However, *(i)* compaction of the crystal pile has been merely inferred from plastic deformation of plagioclase crystals only, and *(ii)* the strength and efficiency of compaction to induce melt transport are poorly constrained. The typical coarse-grained textures of oceanic gabbros impede the analyses of a statistically significant number of grains (in a single thin section) to obtain reliable microstructural quantifications. Additionally, slow- to ultraslow-spreading oceanic crust is mainly studied at OCC where crystal-plastic deformation related to detachment faulting commonly overprints primary magmatic fabrics. This strongly challenges sampling of pristine gabbros recording magmatic processes, thereby explaining the poorly documented symmetry of magmatic fabrics at slower-spreading ridges (Cheadle and Gee, 2017).

In this contribution, we provide detailed microstructural analyses of olivine gabbros from the in situ section of ultraslow-spreading oceanic crust cored in IODP Hole U1473A at the Atlantis Bank OCC. Our sample suite was selected from the deepest section of the hole where minor crystal-plastic deformation overprint is recorded, and primary magmatic features are preserved. Electron Backscattered Diffraction (EBSD) allows us to quantify grain deformation and mineral fabric orientation, strength, and symmetry. Such microstructural quantifications were determined for both coarse- and fine-grained olivine gabbros. EBSD analyses of fine-grained intervals permit to define Crystallographic Preferred Orientations of plagioclase from an ultraslow-spreading crust, and to overcome the poor statistics related to the small number of grains measured in coarse-grained samples. Microstructural analyses are presented here and are used to *(i)* constrain the extent of compaction in the Atlantis Bank lower oceanic crust, and *(ii)* assess the control of compaction on melt extraction from the crystal mush. In a recent geochemical study on the same sample suite, we showed that the melt extracted from the crystal mush segregated in discrete melt-rich zones that ultimately crystallized the fine-grained olivine gabbro cumulates ubiquitously observed throughout Hole U1473A (Ferrando et al., 2021). Here, we investigate the ability of compaction to accumulate melts in these discrete zones.

2. The Atlantis Bank and IODP Hole U1473A

The Atlantis Bank consists of a ~ 5000 m-high dome covering an area ~ 37 km-long and ~30 km-wide (e.g., Dick et al., 1991a; Baines et al., 2003; Hosford et al., 2003). It is located at the inside corner of the intersection of the Atlantis II transform and the ultraslow-spreading SWIR (57°E; Fig. 1a; average spreading rate 14 mm/yr; Dick et al., 1991a). The Atlantis Bank OCC lies on the high transverse ridge that runs parallel to the transform valley and that was created by a 7.5 Myr long transtension phase on the Atlantis II Transform fault due to a spreading direction change at ~19.5 Myr. Transtension substantially uplifted and shifted the Atlantis Bank to its present-day location ~93 km south of the SWIR axis (Fig. 1a; e.g., Dick et al., 1991a; Baines et al., 2007, 2008; Palmiotto et al., 2013).

The Atlantis Bank OCC exposes lower oceanic crust and upper mantle denuded by the continuous exhumation event (review in Dick et al., 2019a). Site surveys, geological mapping and drilling (e.g., Dick et al., 1991b, 2000; Pettigrew et al., 1999; MacLeod et al., 1998, 2017; Arai et al., 2000; Matsumoto et al., 2002) revealed that the uplifted lower crust is composed of massive gabbros (dominantly olivine gabbro), emplaced by continuous magmatic activity over ~3 Myr (from ~13.4 to ~10.5
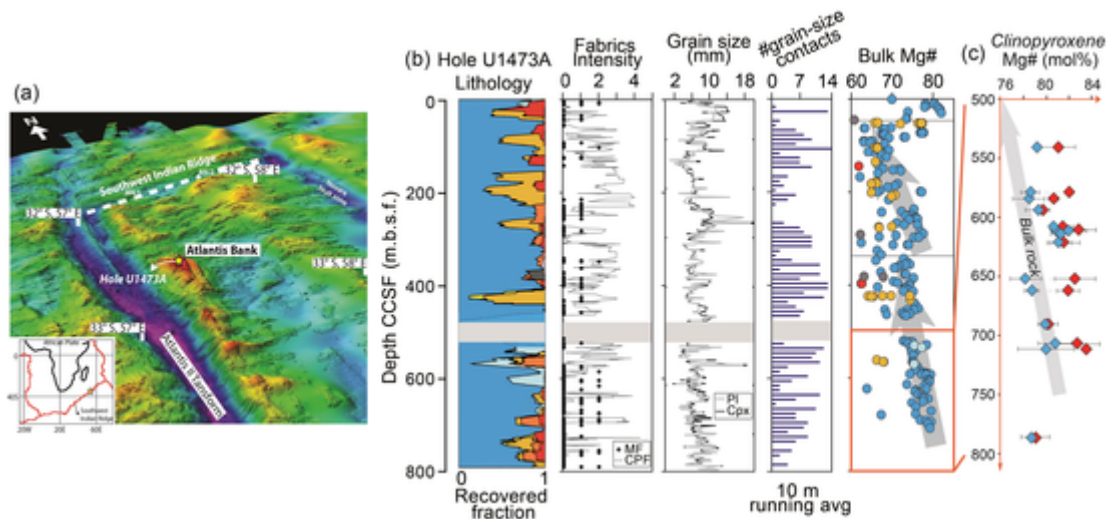
Fig. 1. (a) Location of the Atlantis Bank OCC and of IODP Hole U1473A drilled during Expedition 360 on its flat top (modified after MacLeod et al., 2017). (b) Downhole lithologies and associated textures (from left to right: magmatic (black dots) and crystal plastic fabrics (grey line, running average); Pl (light grey line) and Cpx (black line) grain sizes (mm); number of grain-size contacts, given as 10 m-running average), and downhole bulk-rock Mg# (dot colors represent the lithology as reported in the first column 'Hole U143A Lithology'). Colors correspond to the lithology: dark blue - olivine gabbro, light blue – gabbro, yellow - disseminated oxide gabbro, orange - oxide-bearing gabbro, red - oxide gabbro, grey - diabase. The grey horizontal bar represents the drilled interval with no recovery (see MacLeod et al., 2017); (c) Composition of cores of Cpx crystals (average per sample) in the studied interval from 500 to 800 mbsf; Red diamonds represent coarse-grained Cpx, while blue diamonds display the composition of fine-grained crystals. (For interpretation of the references to colour in this figure legend, the reader is referred to the web version of this article.)

Myr) at approximately 5–6 km-depth beneath the ridge axis (Baines et al., 2008; Rioux et al., 2016). The >4 km-thick magmatic crust estimated in this region (e.g., Minshull et al., 1998) is exceptional for the overall thin and discontinuous lower oceanic crust observed along the SWIR (e.g., Cannat et al., 1999, 2006; Muller et al., 1999); this was attributed to local high melt supply from an unusual portion of fertile mantle (Yu and Dick, 2020). The gabbroic massif was drilled on top of the dome in two ODP Holes 735B and 1105A, and the recent IODP Hole U1473A. Overall, the stratigraphy of the three Holes documents adcumulate gabbros showing various 200 m to 450 m-thick major igneous units depicted by upward decrease in bulk Mg#, Ca#, and Cr and Ni concentrations (Fig. 1b; Dick et al., 2000, 2019a; MacLeod et al., 2017).

IODP Hole U1473A (IODP Expedition 360; MacLeod et al., 2017; Dick et al., 2019b) penetrated ~810 meters below sea floor (mbsf), sampling mainly olivine gabbros (76.5%), less abundant disseminated-oxide gabbro (containing 1–2% oxide; 9.5% of recovery), oxide gabbro (>5% oxide; 7.5% of recovery), gabbro (sensu stricto; 5% of recovery), and minor felsic veins (1.5%) (Fig. 1b). The cored oceanic crustal section is characterized by a ~ 560-m thick zone, from ~15 to 585 mbsf (Fig. 1b), with frequent crystal-plastic deformation overprinting the primary magmatic fabrics. Extensive crystal-plastic deformation is observed throughout the Hole, with local ultramylonites mostly present within the uppermost ~300 m. The intensity of crystal plastic deformation decreases downhole, where magmatic features are best preserved (MacLeod et al., 2017; Zhang et al., 2020). Accordingly, primary magmatic fabrics (MF) are identifiable in ~40% of the Hole with the majority of gabbroic rocks displaying random orientation of primary igneous minerals (MF = 0, Fig. 1b; see MacLeod et al., 2017), while discrete intervals of about 80 cm thickness maximum are characterized by weak (MF = 1) to moderate (MF = 2) MF defined by the shape preferred orientation (SPO) of elongated laths of euhedral to subhedral tabular plagioclase (Pettigrew et al., 1999).

Olivine gabbros display highly variable mineral grain-size ranging from fine- and medium- (0.2–1.5 mm) to coarse-grained crystals (2–15 mm) (Fig. 1b; MacLeod et al., 2017; Dick et al., 2019b). Grain-size contacts can be related to local intense crystal-plastic deformation (sheared contacts in Fig. 2a), leading to extensive grain-size reduction after dynamic recrystallization (see MacLeod et al., 2017). Throughout

IODP Hole U1473A, however, gabbros are locally not plastically deformed (Fig. 1b) and thus preserve their primary characteristics. Where crystal plastic deformation is absent or of minor intensity, grain-size contacts are of magmatic origin(Fig. 2b). Primary magmatic contacts between intervals of different grain sizes are commonly observed (121 contacts logged during IODP Expedition 360; MacLeod et al., 2017; one contact on average every ~4 m of recovered core) and were identified throughout Hole U1473A at all depths (Fig. 1b). Grain-size contacts are mostly irregular and "patchy", i.e. showing coarse-grained domains included into a fine-grained matrix, with variable thickness of fine- (or medium-) and coarse-grained intervals (Fig. 2b; MacLeod et al., 2017).

Shipboard bulk rock analyses highlighted three principal chemical units each showing upward chemical differentiation (Fig. 1b), which are separated by two chemical discontinuities at ~60–90 mbsf and ~350 mbsf (Fig. 1b; MacLeod et al., 2017). In the deepest chemical unit of Hole U1473A, within the depth interval 500–800 mbsf (below the 'no recovery' interval; Fig. 1), the 96% recovery sampled olivine gabbros showing minor crystal-plastic overprint. These olivine gabbros commonly preserve their primary magmatic textures and grain-size variations and thus represent the best candidates to investigate the primary magmatic fabric.

3. Sampling and petrography

The samples investigated herein were selected from the olivine gabbros described in Ferrando et al. (2021), and sampled from the 500–800 mbsf depth interval in IODP Hole U1473A, where was presented a comprehensive petro-geochemical study of pristine olivine gabbros devoid of crystal-plastic deformation overprint and characterized by primary grain-size variations. Here, we performed petrographic observations and microstructural analyses on 15 selected olivine gabbros (Table 1), all sampled across grain-size contacts.

The magmatic, irregular grain-size variations (Fig. 2b) are characterized by sutured grain-size contacts displaying variable orientations visible in the core-cut surface (Fig. 2b,d) and in whole-round images (Supplementary Fig. S1). Olivine gabbros from both coarse-grained and fine-grained intervals contain assemblages of subhedral to anhedral olivine (Ol), equant euhedral to subhedral and lath-shaped plagioclase

Table 1

List of samples (Full sample name: R = Rotary core barrel; W = working half), mineral modal proportions (olivine = ol; plagioclase = pl; clinopyroxene = cpx; orthopyroxene = opx) and quantified EBSD grain size parameters for crystals of plagioclase, clinopyroxene and olivine; SF = Shape Factor; GOS = Grain Orientation Spread; MGD = Maximum Grain Deformation (maximum Mis2Mean for each detected grain). Full sample names are reported as (360-U1473A-) core-section-interval (in centimeters).

Full sample name	Mineral modal %				EBSD setup			Plagioclase grain analyses					Clinopyroxene grain analyses				Olivine grain analyses		
	Ol	Pl	Cpx	Opx	Analyzed area (mm)	Step size		Mean Area	Mean SF	GOS	Mean MGD	Aspect ratio	Mean Area	Mean SF	GOS	Mean MGD	Mean Area	GOS	Mean MGD
64R-8W, 128–139	6	54	38	2	33 × 19	30	Fine	1.05×10^5	1.59	1.19	4.13	2.77	9.31×10^4	1.76	1.00	3.35	7.77×10^4	1.17	3.84
							Coarse	3.74×10^6	3.17	2.55	12.98	3.04	4.93×10^6	8.47	1.80	11.33	1.89×10^6	5.76	20.15
65R-6W, 98–108	7	56	34	3	29 × 18	17	Fine	1.12×10^5	1.78	0.92	4.05	3.10	6.50×10^4	1.94	0.68	2.75	8.32×10^4	1.10	3.98
							Coarse	2.52×10^6	3.69	1.79	11.34	3.47	1.85×10^6	7.27	1.60	9.35	3.98×10^6	4.10	15.94
67R-3W, 73–77	5	63	31	1	35 × 19	20	Fine	1.32×10^5	1.77	0.95	4.33	3.48	9.79×10^4	2.09	0.88	3.37	8.92×10^4	0.98	3.41
							Coarse	2.71×10^6	3.61	1.47	9.9	3.85	3.60×10^6	8.6	1.53	9.92	3.80×10^6	4.45	17.11
67R-5W, 53–56	5	56	36	3	28 × 19	18	Fine	9.85×10^4	1.71	0.70	2.94	2.99	7.18×10^4	1.98	0.51	2.03	6.21×10^4	0.90	3.15
67R-5W, 60–63					26 × 19	30	Coarse	3.10×10^6	2.88	2.04	9.73	3.64	3.41×10^6	5.82	1.40	8.49	1.55×10^6	2.81	9.00
67R-6W, 4–9	6	63	29	2	37 × 18	18	Fine	8.85×10^4	1.71	0.83	3.61	2.98	1.02×10^5	2.2	1.02	3.91	1.14×10^5	1.54	4.71
							Coarse	2.61×10^6	4.24	1.66	10.28	2.70	2.22×10^6	11.43	2.42	11.33	1.55×10^6	2.30	9.84
67R-8W, 4–8	7	63	28	2	36 × 18	35	Fine	1.18×10^5	1.64	1.52	5.05	2.76	8.69×10^4	1.74	1.09	3.6	1.04×10^5	1.43	4.36
							Coarse	3.22×10^6	2.87	2.26	11.88	3.84	2.05×10^6	5.51	2.30	12.29	1.54×10^6	2.86	12.13
68R-5W, 64–70	6	58	35	1	36 × 20	20	Fine	1.25×10^5	1.7	0.66	2.89	2.97	1.14×10^5	2.1	0.67	2.57	9.39×10^4	0.70	2.60
							Coarse	2.79×10^6	3.18	1.54	9.07	3.44	2.13×10^6	6.55	0.98	6.37	2.70×10^6	2.71	11.55
74R-7W, 106–113	5	48	46	1	22 × 19	25	Fine	1.36×10^5	1.71	1.02	4.01	3.53	1.13×10^5	2.06	0.91	3.55	1.08×10^5	1.30	3.98
							Coarse	3.03×10^6	3.01	1.70	11.02	3.66	5.47×10^6	10.45	1.17	11.91	2.52×10^6	2.59	15.91
78R-7W, 68-74a	8	66	25	1	28 × 18	30	Fine	1.21×10^5	1.63	0.73	2.74	3.04	7.48×10^4	1.74	0.65	2.28	8.64×10^4	1.18	3.57
							Coarse	4.55×10^6	2.76	1.27	8.57	3.46	2.87×10^6	7.10	0.80	6.45	1.85×10^6	4.44	14.58
79R-8W, 17–21	6	53	38	3	35 × 20	20	Fine	1.21×10^5	1.74	0.64	2.82	3.10	9.29×10^4	2.06	0.67	2.79	8.59×10^4	1.32	4.07
80R-4W, 143–146	13	60	24	3	29 × 19	30	Fine	1.32×10^5	1.68	0.48	2.03	3.40	1.31×10^5	1.98	0.64	2.22	1.36×10^5	0.71	2.39
							Coarse	2.42×10^6	2.83	0.95	6.23	3.27	2.64×10^6	6.83	1.12	5.55	1.85×10^6	2.24	7.19
80R-8W, 81–87	12	51	36	1	37 × 18	20	Fine	1.50×10^5	1.73	0.78	3.61	3.30	1.71×10^5	2.26	0.85	3.64	1.35×10^5	1.04	3.74
							Coarse	3.31×10^6	2.96	0.99	8.03	3.55	1.88×10^6	5.19	1.13	7.30	2.00×10^6	2.05	9.05
83R-4W, 118–124	5	72	21	2	37 × 19	20	Fine	1.14×10^5	1.67	0.51	2.30	2.99	9.68×10^4	1.91	0.47	2.31	8.75×10^4	0.79	2.77
							Coarse	6.06×10^6	3.68	0.99	6.88	3.17	2.06×10^6	8.30	0.85	6.03	2.49×10^6	2.84	8.00
89R-6W, 95–99	22	48	29	1	34 × 16	30	Fine	1.49×10^5	1.61	0.77	2.94	3.21	8.72×10^4	1.82	0.70	2.36	9.26×10^4	1.33	3.62
							Coarse	5.24×10^6	2.85	1.39	8.47	4.45	7.61×10^6	9.07	1.40	10.07	1.44×10^7	3.61	13.64

(Pl), and granular to poikilitic clinopyroxene (Cpx). Mineral SPO is overall random or very weak resulting mostly in isotropic textures at the macroscopic scale (Shipboard data; MacLeod et al., 2017; Fig. 2c). Coarse-grained domains show variable thickness and are embayed by domains of fine-grained olivine gabbro (Fig. 2b). Textures of coarse-grained olivine gabbro are predominantly subophitic (Fig. 2d), with plagioclase chadacrysts showing lobate contacts against clinopyroxene oikocrysts. Along the grain-size magmatic contacts, coarse-grained minerals are locally truncated (mainly Pl) and commonly display lobate contacts against fine-grained counterparts.

The subophitic textures of coarse-grained olivine gabbros are characterized by overall randomly oriented Pl crystals (Fig. 3a), subhedral to anhedral Ol and large anhedral (Fig. 3b) to poikilitic Cpx locally embaying Pl chadacrysts (Fig. 3a,c). Coarse Pl crystals have characteristic elongated shapes (Fig. 3a-c). Tapered (mechanical) twins are commonly observed in coarse Pl crystals, especially in contact or nearby Cpx crystals (Fig. 3a). Elongated Pl with the highest aspect ratios (long axis/short axis) are locally bent (Fig. 3a,b) and display subgrain boundaries perpendicular to the crystal elongation direction (Fig. 3a). At the

contact with coarse Cpx, these high aspect ratio Pl tend to bend around the Cpx crystals (Fig. 3b). Pl grain boundaries are serrate at contacts with other coarse Pl, resulting in crystal interlocking (Fig. 3a). Coarse Ol crystals show well-developed subgrain boundaries. Large oikocrysts of Cpx show undulose extinction displaying minor subgrain boundaries.

The fine-grained intervals display granular textures (Fig. 2d) with euhedral to subhedral crystals showing smooth, equilibrated crystal boundaries (Fig. 3a,d). Fine-grained Pl crystals have generally rounded shapes or are slightly elongated with low aspect ratios and show scarce or lacking twins (Fig. 3d). Subgrain boundaries are not developed in fine-grained Ol crystals (Fig. 4e,f). Fine-grained Cpx crystals occur mostly as interstitial grains (Fig. 3a,d) and show undulose extinction in only a few grains, without remarkable subgrain boundaries (Fig. 4g,h).

4. Methods

Microstructures were analytically characterized on whole thin sections by Electron Backscattered Diffraction (EBSD) technique using the Field Emission Gun CamScan X500FE CrystalProbe facility at Géo-
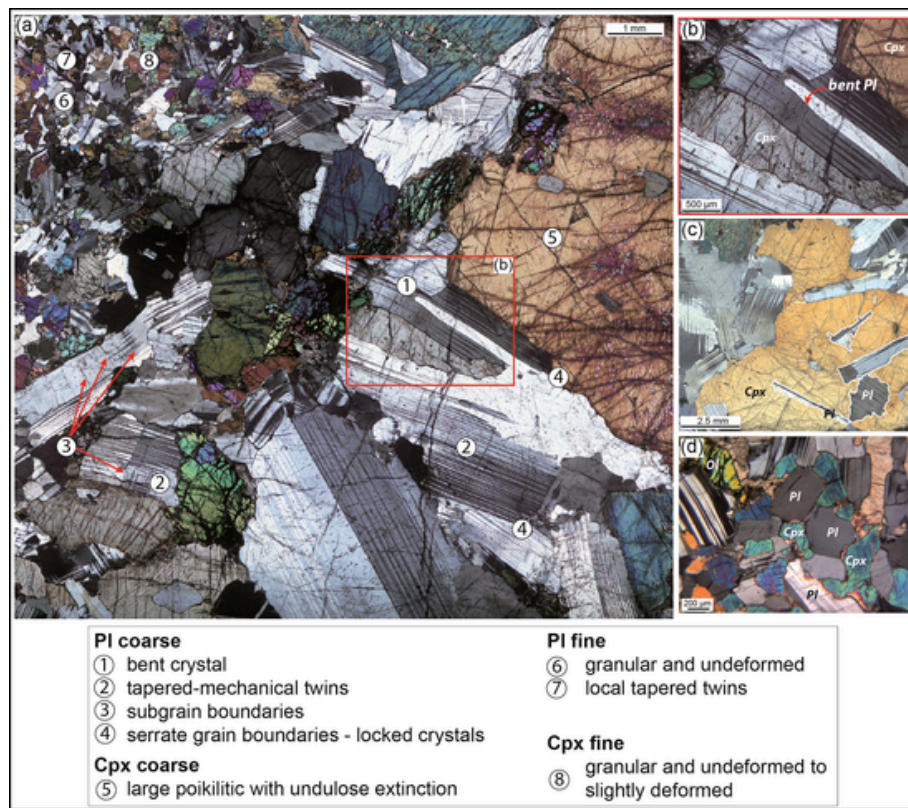
Fig. 3. Textures of coarse- and fine- grained olivine gabbros. (a) Sample 360-U1473A-66R-7 W, 12–18 cm best illustrating the characteristic textures of both coarse- and fine-grained olivine gabbros (numbers indicate the microstructures listed at the bottom of the figure); (b) Close-up showing a bent Pl around Cpx; (c) Large poikilitic clinopyroxene oikocryst embay plagioclase showing corroded grain boundaries in sample 74,360-U1473A-64R-4 W, 19–24 cm; (d) Undeformed fine-grained olivine gabbro with typical granular textures.

sciences Montpellier (University of Montpellier). Diffraction patterns were recorded by the Nordlys Nano EBSD CCD Camera, installed perpendicular to the incident electron beam, with an angular resolution of 0.3°. Operating conditions were a 20 kV accelerating voltage, a 5 nA beam current, and a working distance of 25 mm under low vacuum conditions (2 Pa of gaseous Nitrogen). Areas of ~35 × 20 mm were mapped for each sample at different sampling step sizes ranging between 17 μm to 35 μm depending on the minimum grain size of the analyzed sample (Table 1). EBSD raw data were first processed using the CHANNEL5 software from Oxford Instruments HKL to remove isolated single pixels and to increase the indexation rate by filling automatically the non-indexed pixel having up to 8 indexed neighbors. Indexation rates are ~95% or more. Grain, textural and Crystallographic Preferred Orientation analyses of EBSD data were performed using MTEX (version 4.5.2), an open-source MatLab® toolbox that allows quantitative microstructural analyses covering a wide range of properties (e.g., Hielscher and Schaeben, 2008; Mainprice et al., 2014). Single grains were reconstructed by automatically selecting adjacent pixels having misorientations <10° (misorientation angle >10° mark grain boundaries). Systematic grain identification errors in plagioclase caused by crystal twinning were corrected by automatically merging crystals having misorientation angle >178° between pixels. The mineral modal abundance of each thin section was quantified by EBSD mapping (Table 1).

4.1. Grain analyses

We performed grain analyses of Pl, Ol and Cpx crystals. The identification of grains using MTEX enables to quantify a series of textural parameters describing the morphology and the intra-crystalline deformation of each detected grain. We determined the number of grains and

the area of each grain (in μm^2) by multiplying the number of pixels in the considered grain by the area of one pixel (depending on the analytical step-size). Based on thin section observations, the diameter of fine-grained crystals ranges from <0.1 mm to ~0.8 mm and averages out to ~0.4–0.5 mm (MacLeod et al., 2017; Ferrando et al., 2021), hence we set a threshold of ~10^6 μm^2 grain area to distinguish the fine-grained (<10^6) from coarse-grained (>10^6) crystals.

To quantify the tortuosity of the grain perimeter (i.e., morphology), we used the shape factor (Mainprice et al., 2014), which corresponds to the ratio between the perimeter of a grain and its equivalent perimeter (perimeter of a circle that has the same area as the considered grain). High values of shape factor indicate anhedral crystals, as for example interstitial or poikilitic, while low values are typical of granular textures.

Intra-crystalline deformation is described by the Mis2Mean parameter that quantifies the misorientation of each pixel within a single grain with respect to the mean orientation of the grain (Mainprice et al., 2014). We determined the average Mis2Mean for each detected grain, hereafter referred to as 'Grain Orientation Spread (GOS)'. Because GOS is the average misorientation of all pixels in a single grain, the misorientation of just a few pixels is over-weighted in fine-grained crystals and under-weighted in coarse crystals; therefore, the misorientation can be overestimated for fine-grained crystals and underestimated for coarse crystals. To overcome this analytical bias, we also computed the maximum Mis2Mean for each detected grain ('Maximum Grain Deformation', MGD).

Grain area, Shape factor, GOS and MGD of Pl, Ol and Cpx crystals are reported in Table 1.
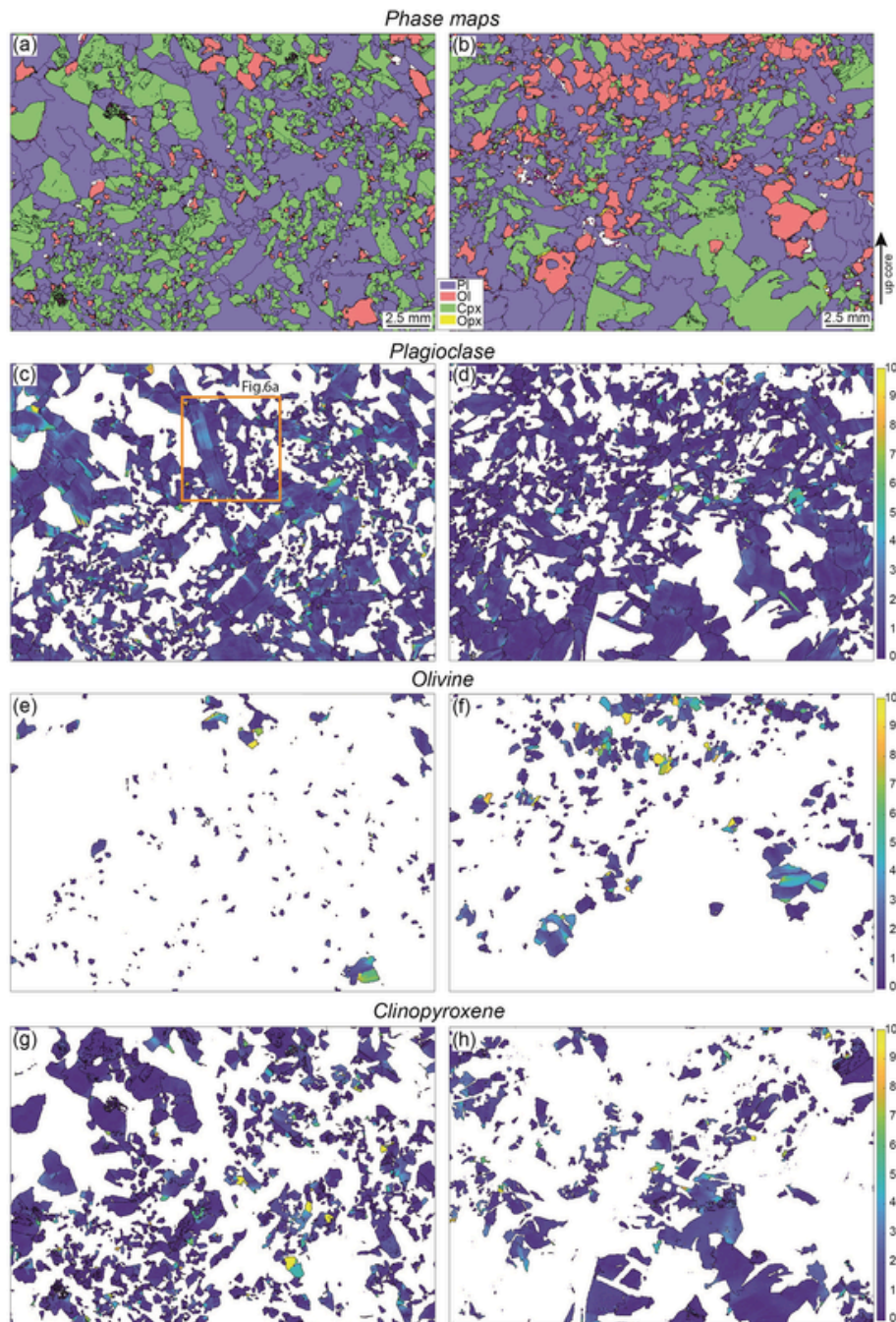
Fig. 4. Phase maps (a-b) and Mis2Mean maps (c-h) obtained by Electron Backscattered Diffraction analyses. We report the examples of two representative samples: (a, c, e, g) are maps of sample 360-U1473A-68R-5 W, 64–70 cm and (b, d, f, h) of sample 360-U1473A-80R-4 W, 143–146 cm. Colour coding is reported in the legend and the scale of Mis2Mean on the right. Mis2Mean maps of Pl, Ol and Cpx are shown in (c-d), (e-f) and (g-h), respectively.

4.2. Crystallographic preferred orientation

To measure representative Crystallographic Preferred Orientation (CPO) of mineral phases, a statistically significant number of grains is needed (arbitrarily set to 100 grains in Satsukawa et al., 2013). In olivine gabbros, this requirement is mostly satisfied by Pl (see mineral grain number in Table 2). For each sample presenting a grain-size contact, two subsets were selected in MTEX, one of coarse- and one of fine-grained interval, to evaluate the fabric characteristics of coarse-grained and fine-grained Pl separately. Pl CPO were determined for a total of 12 samples. While most coarse-grained intervals has a total number of grains <60, in two samples the coarse-grained portion contains at least ~80 grains (see Table 2). The latter, exclusively, were selected for reli-

able CPO evaluation. CPO were determined using all pixels and are presented in equal-area, lower hemisphere stereographic projections (pole figures).

The fabric strength of CPO was determined by the J-index (J) of the orientation distribution function (ODF; e.g., Bunge, 1982; Mainprice et al., 2014). Because the J becomes unrealistically high for aggregates <~1000 grains (e.g., Skemer et al., 2005; Satsukawa et al., 2013), we also calculated the M-index (M) that is less dependent on the number of grains (Skemer et al., 2005). The M will be here used preferentially for coarse-grained intervals with ~80 grains analyzed. The J has a value between 1 for a random distribution (isotropic fabrics) and infinity for single crystal orientation, whereas M varies from 0 for isotropic fabrics, to 1 for single crystal orientation.

Table 2

Strength of fabrics and Pl CPO parameters. Short name of samples are reported as core-section (see Table 1 for full sample name). The pfJ-index is the strength of single pole figures (Mainprice et al., 2014). Short name as in Table 1.

Short name	Fine/coarse	n° grains	M-index	J-index	pfJ-index [100]	(010)	(001)	BA-index	L# e1/e2 [100]	F# e1/e2 (010)	K-factor [100]	(010)
64–8	Fine	1467	0.032	4.33	1.20	1.22	1.24	0.42	1.31	1.42	1.83	3.54
65–6	Fine	1515	0.042	3.26	1.21	1.22	1.15	0.29	1.13	1.51	0.24	1.87
67–3	Fine	1129	0.021	3.35	1.17	1.33	1.13	0.51	1.21	1.34	0.83	0.69
67–6	Fine	2285	0.038	2.86	1.26	1.25	1.09	0.58	1.43	1.26	0.96	0.45
67–8	Fine	1472	0.040	3.03	1.27	1.34	1.08	0.29	1.16	1.60	0.27	1.90
68–5	Fine	1333	0.019	2.94	1.19	1.17	1.12	0.72	1.37	1.06	1.85	0.17
	Coarse	83	0.035	6.13	1.33	1.57	1.28	0.44	1.15	1.43	0.52	0.74
79–8	Fine	1893	0.030	2.33	1.21	1.21	1.05	0.65	1.47	1.20	1.37	0.35
80–4	Fine	1003	0.034	3.47	1.24	1.19	1.17	0.39	1.32	1.34	0.83	2.20
	Coarse	78	0.044	10.85	1.60	1.73	1.6	0.49	1.34	1.33	0.52	0.62
80–8	Fine	684	0.010	4.37	1.20	1.28	1.16	0.61	1.31	1.24	3.14	1.23
83–4	Fine	1197	0.039	3.1	1.37	1.22	1.14	0.73	1.79	1.14	2.16	0.29
67–5	Fine	2203	0.065	2.65	1.29	1.32	1.03	0.38	1.40	1.69	0.65	1.72
78–7	Fine	1002	0.040	3.57	1.28	1.16	1.18	0.47	1.43	1.33	1.24	1.75

The CPO pole figure symmetry can be quantified using the eigenvalues ($e_1 \geq e_2 \geq e_3$, with $e_1 + e_2 + e_3 = 1$) of the normalized orientation tensor for each principal crystallographic axis or poles to planes (Mainprice et al., 2014 and references therein). The eigenvalues were here used to evaluate whether the orientation distribution of each crystallographic axis is random or shows point (or cluster) to girdle concentrations. Due to the tabular shape of euhedral Pl crystals, their (010) planes organize parallel to the foliation plane and [100]-axis parallel to the lineation direction (e.g., Morales et al., 2011; Holness et al., 2017; Satsukawa et al., 2013; Vukmanovic et al., 2018; Bertolett et al., 2019). Hence, we focused on the Pl [100] axis and the Pl (010) plane to define, respectively, the sample lineation and the magmatic foliation. More-

over, the Pl (010) planes best describe the foliation even in samples where its observation at the thin section scale is not obvious. On this basis, we computed the BA-index (BA), representative of the CPO symmetry of the Pl [100] and (010) (Satsukawa et al., 2013; Mainprice et al., 2014); the BA value is 0 when the (010) pole figure is a perfect point maximum and the [100] pole figure is a perfect great circle girdle (axial-B pattern; Satsukawa et al., 2013), and it is 1 when [100] is a perfect point maxima and (010) shows girdle distribution (axial-A pattern; Satsukawa et al., 2013). Intermediate values of BA (~0.5) are defined by point maxima of both [100] and (010) pole figures (P-type pattern; Satsukawa et al., 2013). We also calculated the K-factor (K) as determined by Woodcock (1977) to quantify the orientation distribution of single pole figures (girdles for $0 \leq K < 1$ and clusters for $1 < K \leq \infty$); the K was determined for Pl [100] in order to quantify the strength of lineation in coarse- and fine-grained intervals of the studied samples. Additionally, we calculated the ratio of the maximum to intermediate eigenvalues of [100] and (010) to determine the strength of lineation (L# = $e_{1[100]}/e_{2[100]}$) and foliation (F# = $e_{1(010)}/e_{2(010)}$), respectively (following Yaouancq and Macleod, 2000 and Cheadle and Gee, 2017). The latter allowed us to best compare our data with published Pl CPO from other geological settings (i.e., slow-spreading and fast-spreading oceanic crust, and continental layered mafic intrusions; e.g., Cheadle and Gee, 2017).

Indices of Pl fabric strength (i.e., *J*, M and pf*J*) and Pl CPO symmetry (i.e., BA, K, L# an F#), together with the number of grains detected, are reported in Table 2.

5. Results

5.1. Quantitative microstructural description

Mineral modal abundances are homogeneous in coarse- and fine-grained intervals of a single sample, whereas they slightly vary between samples from different depths (Table 1, Fig. 4a,b). In contrast, the morphology and intra-crystalline microstructures of coarse-grained crystals differ systematically from those of fine-grained crystals in all samples (see also *Sampling and Petrography*).

Elongated, coarse Pl crystals have lobate and serrate grain boundaries resulting in high values of shape factor, whereas fine-grained granular Pl crystals show low shape factors, consistent with smooth grain boundaries (Fig. 5a: example of shape factor variations in a single sample). Similarly, the poikilitic habit of coarse Cpx crystals is illustrated by higher shape factor compared to granular fine-grained Cpx crystals (Fig. 5b). On average (per sample), shape factors of coarse-grained Pl and Cpx range from 2 to 5 and 5 to 11.5, respectively, whereas shape factors of all fine-grained crystals are ~2 (Fig. 5c).
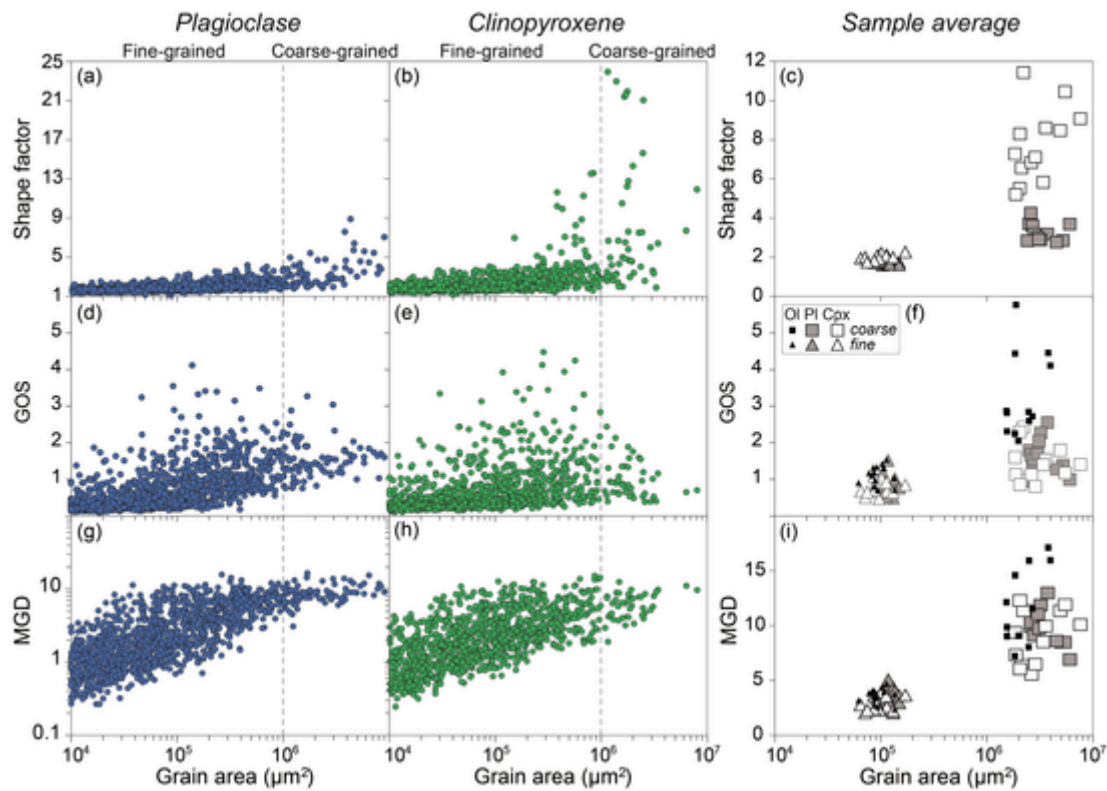
Fig. 5. Shape factor and misorientation parameters, i.e. Grain Orientation Spread (GOS) and Maximum Grain Deformation (MGD), of Pl (a, d, g) and Cpx (b, e, h) in sample 360-U1473A-68R-5 W, 64–70 cm (see relative EBSD maps in Fig. 4), and all averages per sample for Ol, Pl and Cpx (c, f, i). In c), f), i) the grain area is the average grain area per sample. Variations of the parameters are similar in all studied samples, although here we report the details for only one representative sample. All parameters were obtained by grain analyses of the EBSD data (see text for further details). A threshold of grain area of 10^6 μm² was set to distinguish fine-grained ($<10^6$ μm²) from the coarse-grained counterparts.

In Fig. 4(c-h) we report EBSD maps of intra-crystalline misorientation (Mis2Mean) for two representative samples and in Fig. 5(d-i) GOS and MGD are provided for individual grains in a single sample and as average values for all samples.

EBSD data reveal the occurrence of two types of coarse Pl crystals: *(i)* elongated crystals (long dimension in the [100] crystallographic direction) with high aspect ratios and displaying well-developed subgrain boundaries (Figs. 4c, 6a,c); *(ii)* subhedral crystals with lower aspect ratio and irregular grain boundaries, and showing zonation of intra-crystalline misorientation determined by higher Mis2Mean at the crystal rim compared to the relative core (Fig. 4d). To further quantify the misorientation in single grains, we selected misorientation profiles parallel to the long dimension of Pl (Fig. 6a-d). Profiles of misorientation angles to the orientation of the pixel at distance 0 mm (beginning of the profile: point a, c, c' in Fig. 6a,c) in coarse Pl crystals reveal that bell-shaped profile portions are separated by 'jumps' (sharp increase or decrease) in misorientation angle (blue profile in Fig. 6b,d). The latter correspond to peaks in the misorientation profiles with respect to the neighboring pixel (red profile in Fig. Fig. 6b,d). These jumps and peaks correspond to subgrain boundaries that develop perpendicular to the long direction of the Pl crystal (Fig. 6a,c), whereas bell-shaped profiles correspond to bent portions of the Pl crystal. Conversely, most fine-grained Pl crystals have homogeneous Mis2Mean and no subgrain boundaries (Figs. 4c,d, 6a), except for a few grains showing intra-crystalline variations in Mis2Mean values. Consistently, flat misorientation profiles are documented in most fine-grained Pl crystals (Fig. 6b).

Coarse Ol crystals display well-developed subgrain boundaries (Fig. 4e,f). The latter are subparallel to each other and are highlighted by jumps and peaks in misorientation profiles (Fig. 6e,f), similarly to those described in coarse-grained elongated Pl crystals. Fine-grained Ol crystals show homogeneous and low Mis2Mean (Fig. 4e,f).

Coarse Cpx crystals display rather low Mis2Mean, although some grains show higher Mis2Mean values (Fig. 4g,h). Fine-grained Cpx crystals also show overall low Mis2Mean, but locally they display higher Mis2Mean (Fig. 4g,h).

Overall, the EBSD microstructural data indicate that coarse-grained crystals show evidence of intra-crystalline deformation whereas the fine-grained crystals are mostly plastically undeformed. This tendency is quantified by a general smooth increase of GOS with increasing grain area in each sample (Fig. 5d-e). Although this tendency is ubiquitous for all mineral phases in all samples (Fig. 5f), variations of GOS in Pl and Cpx in a single sample are scattered for GOS $> 2°$ (Fig. 5d-e). The within-sample trends of MGD also display a positive correlation with grain area (Fig. 5g-h). Notably, the curve of MGD variations (Fig. 5g,h) is steeper in the range of grain area of fine crystals, and then flattens around a value of 10° when the grain size of coarse crystals is reached. All mineral phases show an overall increase in MGD (averages for coarse- and fine-grained crystals) with increasing grain area (Fig. 5i).

5.2. Plagioclase CPO

More than 1000 Pl grains were measured in fine-grained olivine gabbro, allowing us to obtain reliable CPO. A series of representative Pl CPO is reported in Fig. 7. All CPO of coarse-grained intervals were computed in aggregates <100 grains; we show the two CPO with the highest number of measured grains (68R-5 W, 64–70; 80R-4 W, 143–146).

The fabric strength of the studied samples is dominantly weak and characterized by low *J* and M (Figs. 7, 8 and Table 2). These fabrics are similar to those typical of magmatic origin in oceanic crustal systems, and overall fall within the lowest values of compiled *J* of samples from different geological settings (comprehensive database of Pl CPO from Satsukawa et al., 2013). In particular, the observed weak fabric
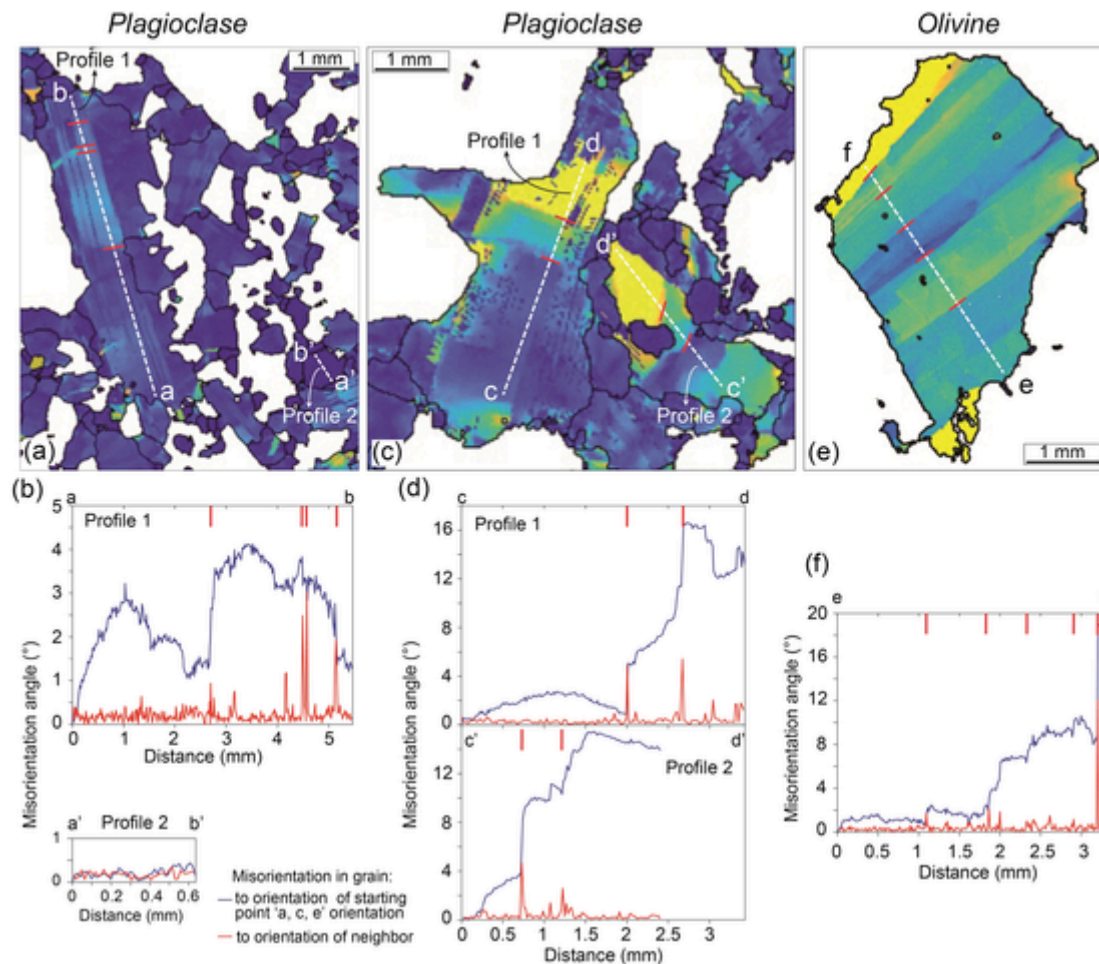
Fig. 6. Two examples of deformed coarse-grained Pl associated with undeformed fine-grained Pl (a, c) and deformed coarse-grained Ol (e) in Mis2Mean EBSD maps; the colour scale is the same as that reported in Fig. 4. White dashed lines trace the misorientation profiles reported in b), d) and f). The red tick-marks highlight the occurrence of subgrain boundaries, which are absent in undeformed grains. Two types of misorientation profiles are presented: the misorientation of each pixel along the profile is measured to the orientation of the pixel at the starting point (i.e., 0 mm; a, a', c, c', e; blue profile), and to the orientation of the neighboring pixel (red profile). (For interpretation of the references to colour in this figure legend, the reader is referred to the web version of this article.)

strengths are comparable with magmatic fabrics documented in gabbros from slow-spreading oceanic crust (Fig. 8), which are generally lower than fabrics of samples from fast-spreading oceanic crust (see also Satsukawa et al., 2013). Although Pl CPO are characterized by low fabric strength (Table 2, Fig. 8), clear patterns of orientation distribution are observed (Fig. 7).

Fine-grained intervals are dominantly characterized by girdle distribution of [100] perpendicular to point maxima of (010), and weak to random orientations of (001). Commonly, the [100] girdle distribution display a point maxima (Fig. 7). Some samples (i.e., 67R-6 W, 4–9; 68R-5 W, 64–70; 79R-8 W, 17–21; 83R-4 W, 118–124) show stronger point distribution of [100] and tend to have girdle distribution of (010) with point maxima (Fig. 7). The variable Pl CPO symmetry is quantified by variable BA and [100] K (Fig. 8). Samples with girdle distribution of [100] and (010) point maxima have axial-B CPO symmetry with low BA (0.15–0.4) and low K (<1). Samples with [100] point maxima (or cluster distribution of [100]; see Fig. 8) and (010) tending to a girdle-like distribution have type-P CPO symmetry with higher BA (up to 0.75) and high K (>1). Consistently, the strength of magmatic lineation L# is variable, showing the highest values in samples displaying type-P CPO symmetry (point maxima of [100]). The strength of magmatic foliation F# is low, ranging between 1 and 1.7 (Figs. 7, 9).

CPO of coarse-grained intervals are mostly random. They show type-P CPO to axial-B symmetry with low to intermediate BA and rather low K (<1.5) (Figs. 7, 8), L# and F# (Figs. 7, 9).

6. Discussion

6.1. Magmatic fabrics as indicative of the geological context

The development and strength of magmatic fabrics in gabbroic rocks vary according to the geodynamic context of formation (e.g., Satsukawa et al., 2013; Cheadle and Gee, 2017). Pl is the most abundant mineral phase constituting gabbroic rocks, and its fabric records the high temperature processes that occurred prior to cooling of the mafic intrusions. Accordingly, Pl fabrics have been widely used to understand the emplacement of crystal mushes in continental (e.g., Higgins, 1991, 2006; Meurer and Boudreau, 1998; Ji et al., 2014; Bertolett et al., 2019) and oceanic crust or ophiolite analogues (e.g., Nicolas and Ildefonse, 1996; Nicolas et al., 2009; Morales et al., 2011; Satsukawa et al., 2013; VanTongeren et al., 2015; Brown et al., 2019); fundamental differences in Pl fabrics were delineated among these geological contexts (Satsukawa et al., 2013; Cheadle and Gee, 2017). While the BA describes the Pl CPO symmetry and provides a single quantification of both foliation and lineation strengths (Mainprice et al., 2014), Cheadle and Gee (2017) proposed that specific correlations between magmatic foliation (F#) and lineation (L#) are indicative of the context of formation of gabbroic rocks (Fig. 9a). Overall, fabrics of Pl from Layered Mafic Intrusions (LMI) (e.g., Higgins, 2006; Holness et al., 2017; Bertolett et al., 2019) are characterized by medium to strong foliations (high F#) and weak lineations (low L#), Pl fabrics from fast-spreading
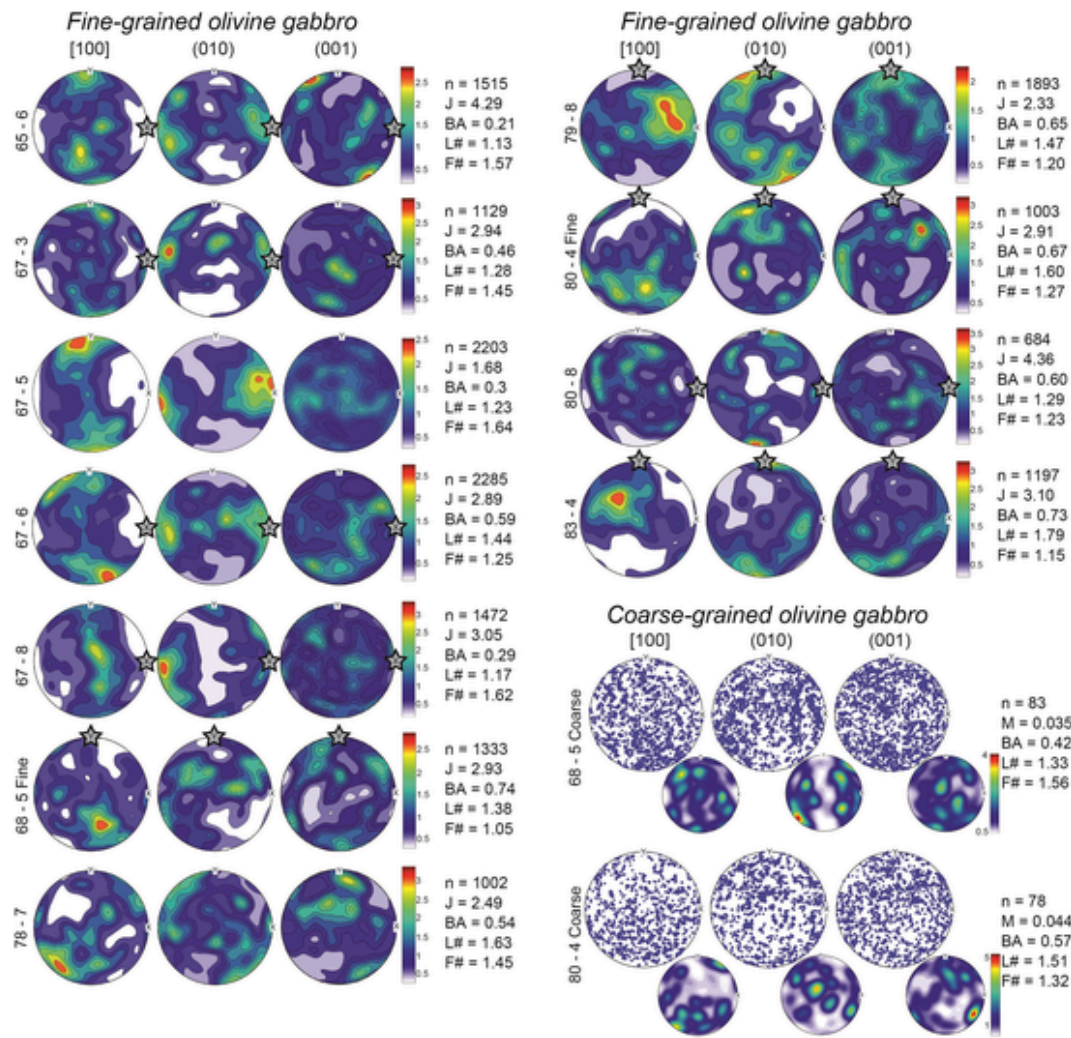
9

Fig. 7. Pl crystallographic preferred orientations (CPO) in olivine gabbros from IODP Hole U1473A. CPO are equal-area, lower hemisphere stereographic projections of all measured pixels; projections are reported in the core reference frame. Pl CPO in fine-grained olivine gabbros are distribution plots; due to the low number of analyzed grains, for coarse-grained olivine gabbros we report scattered plots. Sample names are located on the left of each CPO in the form (360-U1473A-)XX(R)-Y(W) where XX and Y are the section and core numbers, respectively. The stars indicate the vertical of the drill core.

ridges are typically characterized by relatively strong foliations and lineations (medium to high F# and L#) (e.g., MacLeod et al., 1996; Nicolas et al., 2009; Morales et al., 2011; VanTongeren et al., 2015; Brown et al., 2019), and Pl fabrics at slow-spreading ridges show weak foliations (low F#) and variable lineation intensity (low to high L#) (e.g., Satsukawa et al., 2013; Cheadle and Gee, 2017). The strength of these F# and L# structural parameters can be related to physical processes occurring in each geological environment during the formation of the gabbroic bodies, and can be summarized as follows:

1) In LMI, the typically described large magma bodies over 1 km in thickness (e.g., Cashman et al., 2017; Fig. 9b) are filled by long-lived and static crystal mushes (e.g., Bédard, 2015). These large magma reservoirs contain a significant amount of melt (and thus porous space) that allow settling of the crystallizing minerals, in principle without any further perturbation. Crystal settling leads to the development of foliations (e.g., Wager and Brown, 1968; Holness et al., 2017; Ji et al., 2014), while lineations are rare (e.g., Higgins, 2006). Moreover, density-controlled settling can drive crystal segregation during fractional crystallization, leading to the formation of monomineralic layers (e.g., Wager and Brown, 1968; Higgins, 1991). In addition to the settling process, the strength of foliations in LMI also results from compaction of the crystal

mushes. Indeed, continental magmatic systems are composed of multiple crystal mushes distributed throughout the lower crust (Fig. 9b), which can locally be as small as ~150 m-thick (e.g., Holness et al., 2017). The weight of the uppermost denser crystal mushes can drive compaction of the deeper magma chambers, thus reducing the amount of interstitial melt and resulting in the development of stronger foliations (high F#, Fig. 9a; e.g., Holness et al., 2017; Bertolett et al., 2019).

2) At fast-spreading ridges or in fast-spreading ophiolite analogues, the oceanic crust is formed by non-static crystal mushes and a shallow Axial Melt Lens (AML) (e.g., Detrick et al., 1987; France et al., 2009, 2021; Fig. 9c). There, fabrics of oceanic gabbros are strongly controlled by the fast-spreading rates that are accommodated by magmatic accretion (e.g., Boudier et al., 1996; Kelemen and Aharanov, 1998) and continuous lateral flow along the spreading direction (e.g., Nicolas et al., 2009; Fig. 9c). The development of strong foliations (high F#) in those gabbros may result from *(i)* compaction of the crystal pile (e.g., VanTongeren et al., 2015), *(ii)* subsidence along the magma chamber walls prior to its horizontal movement away from the AML (e.g. Nicolas et al., 2009; Brown et al., 2019), and/or *(iii)* upward migration of interstitial melts through a magma mush column, from the lower gabbros to the AML (e.g., Yaouancq and Macleod, 2000).
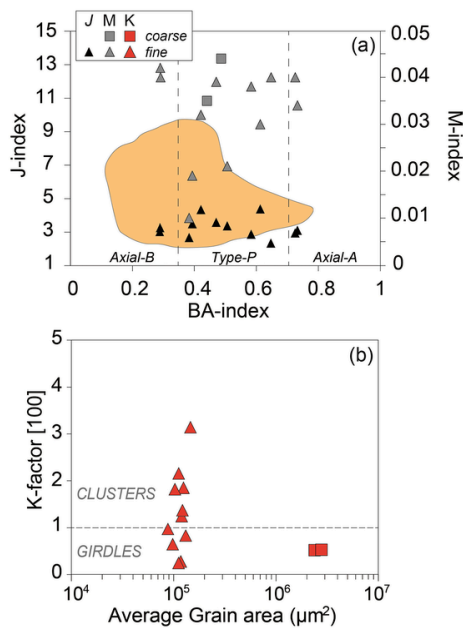
Fig. 8. Indices of Pl fabrics. (a) BA-index vs *J*- and M- indices of the studied fine- (triangles) and coarse-grained (squares) olivine gabbros; the *J*-index of magmatic fabrics developed at slow-spreading environments from the database by Satsukawa et al. (2013) are also reported for comparison (orange field); (b) Average grain area vs K-factor of [100]-axis only; a girdle distribution is considered with K-factor < 1, while cluster distribution refers to K-factors > 1.

Additionally, these foliated gabbros often present weak to medium lineations resulting from crystal alignment during the spreading-related lateral flow of the oceanic lithosphere.

3) The ultraslow- to slow-spreading oceanic crust is built up by ephemeral small magmatic bodies, as evidenced by the absence of quasi-permanent magma lenses (e.g., Sinton and Detrick, 1992; Canales et al., 2017; Fig. 9d). Slow spreading is accommodated by extensive faulting during discontinuous melt supply (e.g. Cannat et al., 2006; Escartín et al., 2008; MacLeod et al., 2009; Blackman et al., 2011). The cooling rates estimated for gabbroic sequences sampled at Atlantis Massif OCC (MAR, Schoolmeesters et al., 2012; Ferrando et al., 2020) and Atlantis Bank OCC (John et al., 2004; Coogan et al., 2007) indicate that those magma bodies cool rather rapidly. The small dimension of magma bodies at slow-spreading ridges, together with their ephemeral character and fast cooling, likely preclude extensive crystal settling and alignment, in turn preventing the development of strong magmatic foliations and, as a consequence, low F# (Satsukawa et al., 2013; Cheadle and Gee, 2017).

Along slow- to ultraslow-spreading ridges, the formation of the oceanic crust at OCCs involves a complex history of discontinuous magmatism and magma emplacement in a continuously uplifted and deforming lower oceanic crust. Consequently, extensive crystal-plastic deformation is commonly recorded in the upper sections of exposed oceanic crust, and in the vicinity of the detachment fault. There, foliations and lineations developed during plastic deformation are able to overprint all primary fabrics (e.g., Allard et al., 2020). An example is shown in Fig. 2a, where a sheared grain-size contact likely developed at the expenses of a pre-existing primary contact. Crystal-plastic deformation and shearing at OCCs are considered to be related to the develop-
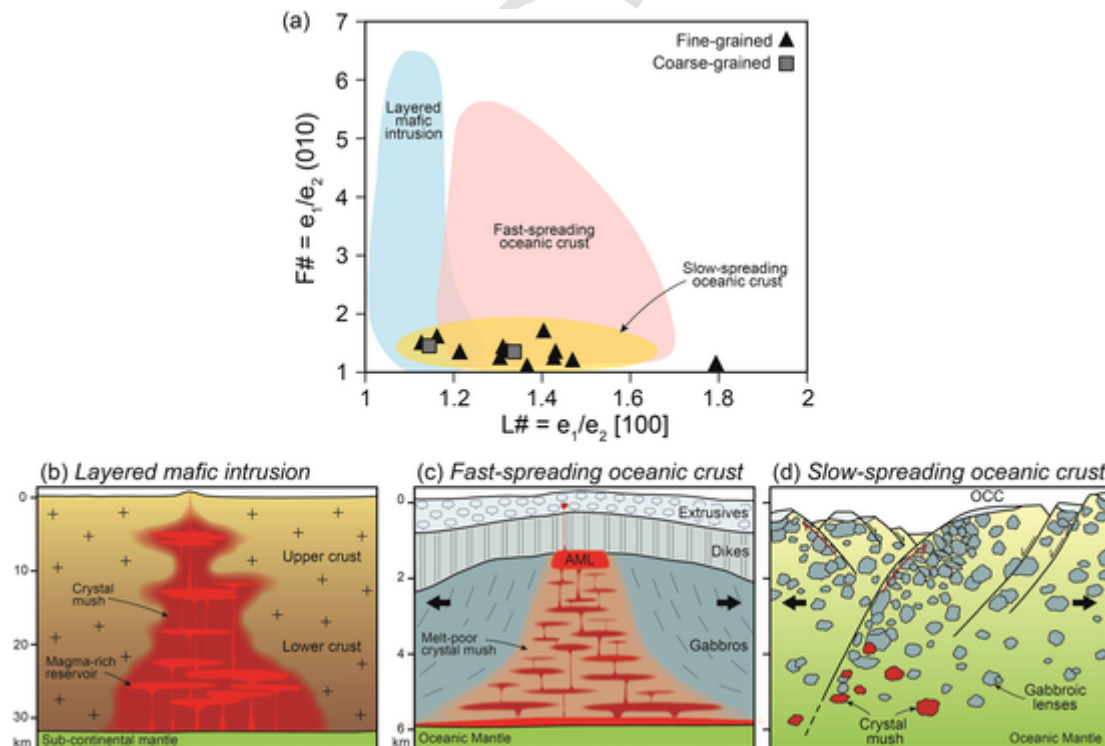

Fig. 9. (a) Strength of plagioclase lineation (L#) and foliation (F#) in gabbros from layered mafic intrusions (blue field), fast-spreading (pink field) and slow-spreading oceanic crust (yellow field) modified after Cheadle and Gee (2017). Results from this study are reported distinguishing fine-grained (triangles) and coarse-grained (squared) olivine gabbros. The bottom of the figure shows sketches of the plumbing system architecture at the three different geological environments: (b) large crystal-mush reservoirs build continental layered mafic intrusion (modified after Cashman et al., 2017); (c) rather large crystal mush zone forms the lower oceanic crust providing magma to the static Axial Melt Lens (AML) below fast-spreading ridges (modified after France et al., 2009); (d) Small and ephemeral crystal mushes cooling to form gabbroic sequences in the lower oceanic crust at slow-spreading ridges. (For interpretation of the references to colour in this figure legend, the reader is referred to the web version of this article.)

ment and continuous activity of the detachment fault (e.g., Miranda and John, 2010; MacLeod et al., 2017; Dick et al., 2019a). This widespread crystal-plastic deformation overprint hampered the documentation of the magmatic fabrics characterizing the slow-spread gabbroic crust, nowadays still poorly constrained. Although IODP Hole U1473A shows widespread crystal-plastic deformation, it decreases in the deepest 200 m of the hole, where it is locally absent (Fig. 1) and primary magmatic features are still present. We emphasize that our sampling strategy focuses on samples that lack evidence of crystal-plastic deformation; accordingly, neoblasts of recrystallized primary mineral phases are nearly absent in all selected olivine gabbros and grain-size reduction related to dynamic recrystallization is not observed. Also, the irregular and locally lobate shape of the studied grain-size contacts cannot result from plastic deformation, which would lead to straight contacts (Fig. 2a).

The magmatic fabrics documented in the studied olivine gabbros are consistent with BA, as well as L# and F# values reported in slow- to ultraslow-spreading oceanic crust (Satsukawa et al., 2013. Cheadle and Gee, 2017), thus confirming that these geological environments are characterized by weak foliations (low F#) and variable lineations (low to high L#) (Fig. 9a). In the following sections, we better constrain the processes driving the development of Pl magmatic fabrics in a section of ultraslow-spreading lower oceanic crust.

6.2. Microstructural features of magmatic deformation at hole U1473A

6.2.1. Intra-crystalline deformation: coarse- vs fine-grained intervals

The studied olivine gabbros display cumulate textures typical of low pressure (~2 kbar) crystallization sequence of a MORB-type melt (e.g., Feig et al., 2006) involving early formation of subhedral Ol and euhedral Pl, further crystallization of elongated Pl followed by crystallization of poikilitic to interstitial Cpx. The occurrence of truncated coarse Pl crystals along the grain-size contacts indicates that the melts forming the fine-grained domains partially dissolved a pre-existing coarse crystal matrix. These grain-size textural relationships have been interpreted as the result of early formation of the coarse-grained intervals and later emplacement of melts forming the fine-grained olivine gabbros (see Ferrando et al., 2021). Poikilitic coarse-grained olivine gabbros formed at higher temperature conditions, whereas the granular textures of fine-grained intervals likely resulted from in-situ adcumulus growth during the progressive cooling of the system, as documented by estimates of equilibrium temperatures (T coarse-grained ~1150 °C, T fine-grained ~1050 °C; Ferrando et al., 2021).

Coarse-grained Ol crystals are characterized by well-developed subparallel subgrain boundaries highlighted in Mis2Mean EBSD maps (Fig. 4e-f) and misorientation profiles (Fig. 6e-f). Their average GOS and MGD are rather high and plot above values obtained for fine-grained Ol crystals (Fig. 5f,i). Coarse-grained Pl crystals commonly display mechanical twins (Fig. 3a) and subparallel subgrain boundaries perpendicular to their elongation direction (Fig. 3a, Fig. 6a-d). Pl crystals with high aspect ratio are often bent against Cpx crystals (Fig. 3a,b). When Pl crystals are interlocked, their contacts are locally lobate (Fig. 3a), as illustrated by relatively high shape factors (i.e., higher than fine-grained Pl; Fig. 5a). At these lobate contacts, deformation at Pl-Pl and Pl-Cpx grain boundaries led to the incipient development of subgrain boundaries and mechanical twins in Pl crystals. On average, coarse-grained Pl crystals have higher GOS and MGD than the fine-grained crystals (Fig. 5f,i). In summary, coarse-grained Pl and Ol are characterized by extensive intra-crystalline deformation. In contrast, coarse-grained Cpx show undulose extinction with a lack of clear microstructural evidence of deformation (i.e., no subgrain boundaries; Fig. 3a); yet, GOS and MGD are higher in coarse-grained Cpx crystals compared to their fine-grained counterparts (Fig. 5e,f,h,i). This suggests that during magmatic processes and high-temperature deformation of the crystal mush, Cpx

was the most rigid mineral phase in the crystal mush, as documented in deformation experiments (e.g., Dimanov and Dresen, 2005).

Ol subgrain boundaries are indicative of dislocation creep at high temperatures. Applying experimental flow laws to partially molten gabbro, Yoshinobu and Hirth (2002) showed that Ol is the weakest phase compared to Pl and Cpx at hypersolidus conditions. Plastic deformation of Ol in the studied coarse-grained olivine gabbros suggest that deformation occurred when the crystal framework was already interlocked, but melt was still present interstitially. Olivine initially accommodated most of the strain by dislocation creep (Fig. 6e,f). Concomitantly, bending of coarse-grained Pl crystals occurred around more rigid Cpx crystals (Meurer and Boudreau, 1998) and diffusion creep led to grain boundary migration and dissolution/precipitation processes in Pl crystals (e.g., Means and Park, 1994; Nicolas and Ildefonse, 1996; Meurer and Boudreau, 1998). At decreasing melt fraction and at near-solidus conditions, when Ol is no longer the weakest phase, Pl also accommodated the strain by dislocation creep, developing subgrain boundaries and mechanical twins (e.g., Meurer and Boudreau, 1998). Therefore, high-temperature intra-crystalline deformation of coarse-grained Ol and Pl likely occurred at hypersolidus conditions when crystals were interlocked and melt was still present in the crystal pile; deformation then proceeded as melt fraction decreased to further deform Pl and, to minor extents, Cpx by dislocation creep.

Conversely, fine-grained minerals show no subgrain boundaries (Figs. 4, 6a,b) and have homogeneous and low Mis2Mean, GOS and MGD (Fig. 5). It was also commonly observed in Hole U1473A that fine-grained intervals show better developed magmatic fabrics (MacLeod et al., 2017). This indicates that fine-grained crystals did not record and are not a result of extensive intra-crystalline deformation. The lack of plastic deformation suggests that the observed magmatic fabrics developed when crystal particles were interacting between them, but the crystal matrix was not yet interlocked (e.g., Ildefonse et al., 1992, 1997). This occurred at relatively high melt fractions (at or above ~30–35% melt fraction; e.g., Van der Molen and Paterson, 1979). Suspension flow persists until grains are fully locked, when deformation starts to be accommodated by the crystal matrix. Once the crystal matrix is locked, the magmatic fabric can only be modified by another mechanism such as pressure solution (e.g., Nicolas and Ildefonse, 1996) or plastic deformation. Interestingly, the lack of deformation in the fine-grained crystals indicate that upon crystallization of the fine-grained intervals, the crystal matrix did not accommodate much deformation even after interlocking of the crystal matrix.

To summarize, deformation in the coarse-grained intervals occurred under hyper- to near-solidus conditions and at decreasing melt fractions; the strain was accommodated by the crystal framework. Conversely, magmatic fabrics in the fine-grained intervals developed when crystals could interact with each other (at or above 30–35% melt fraction) in suspension flow regime, during which deformation was essentially taken up by the melt fraction. The undeformed character of fine-grained crystals indicate that strain was likely minor during the last stages of crystallization.

6.2.2. Pl CPO indicative of crystal mush compaction

The scarce occurrence of aligned Pl crystals, resulting in an overall weak or absent Pl SPO, is in agreement with the isotropic to weak magmatic CPO that characterize the studied olivine gabbros (Figs. 1,2). Although magmatic fabrics are weak, as observed at the macroscopic scale and documented by low J- and M-indices (Fig. 8a), the Pl CPO symmetry of the analyzed samples can be distinguished between coarse-grained and fine-grained intervals.

CPO of coarse-grained Pl show rather low BA- and [100] K-indices (Fig. 8b) suggesting very weak foliation and no lineation. On the other hand, fine-grained Pl typically display type-P CPO patterns (classification from Satsukawa et al., 2013; Fig. 7) with intermediate to high BA- (on average ~ 0.5; Fig. 8a) and [100] K-indices (Fig. 8b), thus indicat-

ing weak foliations and lineations. The lineation is overall oriented sub-horizontal respect to the vertical of the drill core (Fig. 7).

The studied olivine gabbros show no evidence of significant crystal-plastic overprinting (Fig. 4), suggesting that their fabrics were not modified during the exhumation event; thus, the documented Pl CPO are representative of the magmatic emplacement process. Contacts between coarse- and fine-grained intervals are irregular and display no clear evidence of cross-cutting relationships. Additionally, mineral geochemistry indicates that melts forming the fine-grained olivine gabbros originated within the associated coarse-grained olivine gabbros, as evidenced by systematically more evolved compositions of fine-grained intervals respect to their coarse-grained counterpart (Ferrando et al., 2021). Therefore, the grain-size variations showing irregular contacts do not result from multiple melt intrusions but from processes of melt migration and melt extraction within a single crystal mush (see following section; Ferrando et al., 2021). In this scenario, magmatic foliations without well-defined lineations in the coarse-grained olivine gabbros could have developed during crystal accumulation (or settling) or as a consequence of compaction of the crystal pile (or a combination of these two processes). However, the small dimension of magmatic intrusions inferred for the Atlantis Bank OCC (e.g., Dick et al., 2019a) and their fast cooling (John et al., 2004; Coogan et al., 2007) likely hampered the development of foliations by buoyancy-driven crystal settling. This is further supported by the absence of modal layering.

The widespread evidence of intra-crystalline deformation recorded in coarse-grained minerals (subgrain boundaries in Ol and Pl, mechanical twins and bending of Pl crystals, and incipient development of subgrain boundaries in Pl at Pl-Pl and Pl-Cpx contacts; Fig. 3, Fig. 4), together with very weak foliation but no lineation indicate that the crystal mush was deformed by coaxial strain (e.g., Nicolas, 1992; Holness et

al., 2017) as the result of compaction. Moreover, the absence of a well-developed SPO (Fig. 10a,b) suggest that compaction was weak in this gabbroic mush (Fig. 10c), in turn suggesting weak strain.

On the other hand, the Pl type-P CPO patterns observed in the fine-grained intervals (Fig. 7) are typical of foliated rocks with weak to moderate linear fabrics (Satsukawa et al., 2013) that develop in the direction of a magmatic flow (e.g., Brothers, 1964; Benn and Allard, 1989; Higgins, 1991; Nicolas, 1992; Morales et al., 2011). In this context, the orientation of the fabric is a function of the crystal shapes and finite strain (e.g., Ildefonse et al., 1992, 1997). Given the small scale of the fine-grained intervals and their relatively fast crystallization during the exhumation-related cooling of the system (Ferrando et al., 2021), these intervals likely preserved the fabrics related to magmatic flow. During the early stages of magmatic flow, the high melt fraction allowed elongated Pl crystals to be oriented in the direction of melt migration, in turn leading to the development of the weak lineations and foliations observed in the fine-grained olivine gabbros.

6.3. Weak compaction and melt accumulation in the U1473A gabbros

In the lower oceanic crust exposed at the Atlantis Bank OCC, upward trends of mineral and bulk-rock geochemical compositions were interpreted as resulting from upward melt migration through a pre-existing crystal mush (Dick et al., 2000, 2019a; Natland and Dick, 2001; Boulanger et al., 2020; Zhang et al., 2020, 2021; Ferrando et al., 2021). Specifically, within the studied lower section of IODP Hole U1473A, upward decreasing Mg# (Fig. 1b) and Cr_2O_3 concentrations in Cpx, coupled with decreasing bulk-rock Mg# (Dick et al., 2019b), indicate that porous melt transport was associated with progressive evolution of the migrating melt compositions (Ferrando et al., 2021). At the scale of
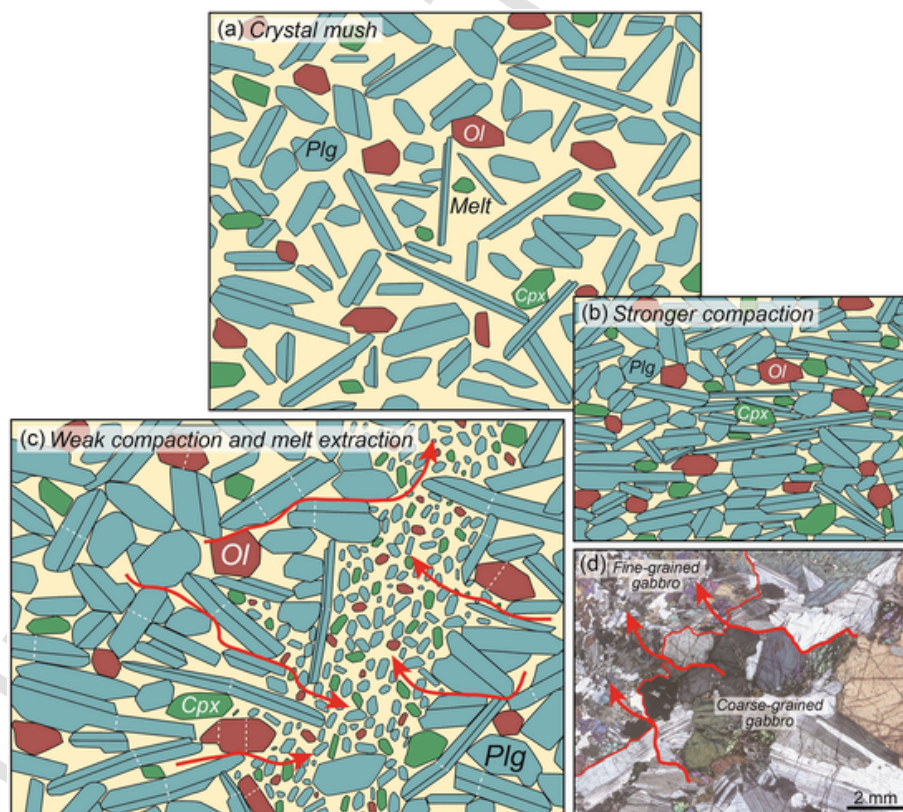

Fig. 10. Sketch illustrating the consequence of compaction of a crystal mush (a) at a slow-spreading environment: (b) strong compaction leads to the development of strong foliations, while (c) weak compaction produces very weak foliation. In the case of gabbros from the Atlantis Bank OCC, microstructures and mineral chemistry point to processes of melt migration, extraction and accumulation: (a) in a pre-existing Ol + Pl ± Cpx melts buoyantly migrate upward; (c) as crystallization proceeds and porosity decreases, compaction of the crystal pile aides melt extraction and accumulation of melts in discrete zones; (c-d) melt segregates in these discrete zones to finally form the fine-grained intervals observed throughout Hole U1473A.

crystal aggregates, porous migration and melt geochemical evolution are recorded in large late-stage poikilitic Cpx, commonly showing geochemical zonation marked by decreasing compatible elements and increasing trace element contents from crystal cores to rims (Meyer et al., 1989; Gao et al., 2007; Lissenberg and MacLeod, 2016; Boulanger et al., 2020; Sanfilippo et al., 2020; Zhang et al., 2020). Consistently, coarse-grained Pl and Cpx in the studied samples display geochemical zonations (Ferrando et al., 2021) that point to progressive geochemical evolution of the crystallizing magma, at decreasing melt mass. Geochemical mineral compositions suggest that cores of coarse-grained Ol + Pl ± Cpx formed a primitive crystal mush, in which the subsequent melt migration occurred (Fig. 10a; Ferrando et al., 2021).

The modal composition of poikilitic minerals can be used as a proxy of the crystal mush porosity, since they likely represent the crystallizing products of melt porous migration (e.g., Meyer et al., 1989; Lamoureux et al., 1999; Coogan et al., 2000; Lissenberg and Dick, 2008). Accordingly, the widespread abundance of poikilitic Cpx (>30% in modal composition on average; Table 1) in the studied coarse-grained intervals suggest that melt migration occurred when an elevated melt fraction was present in the crystal mush (minimum of ~30% melt fraction, i.e., at magmatic and sub-magmatic conditions; see Nicolas, 1992). In this scenario, melt migration was most likely driven by the positive buoyancy of the melts with respect to the crystal framework (e.g., Lissenberg et al., 2019), while compaction of coarse-grained intervals may have had a minor role. This buoyant melt migration was accompanied by crystallization and progressive decrease in porosity, in turn leading to increasing interlocking of crystals.

We emphasize that mineral geochemical analyses indicate that coarse-grained minerals show more primitive chemical compositions compared to the fine-grained counterparts (Ferrando et al., 2021). This indicates that the formation of coarse-grained mineral cores occurred prior to crystallization of fine-grained olivine gabbros. Remarkably, fine-grained minerals show homogeneous chemical compositions similar to the rims of the coarse-grained minerals, thus pointing to a genetic relationship between their parental melts (Ferrando et al., 2021). Based on this genetic relationship, fine-grained mineral compositions were interpreted as resulting from partial extraction of the residual melts from the pre-existing coarse-grained crystal mush into discrete crystal-poor zones (Fig. 10c). These horizons, defined as "melt-rich zones" in Ferrando et al. (2021), were characterized by scarce pre-existing crystal nuclei, which prevented crystal growth and enhanced nucleation at decreasing temperature to form the fine-grained olivine gabbros. Therefore, the fine-grained intervals represent crystallization products of melts extracted from the coarse-grained crystal mush, generating the textural variability that characterizes the studied rocks (Fig. 10d) and is ubiquitously present throughout Hole U1473A.

This process of melt extraction and accumulation in melt-rich and discrete intervals was promoted by compaction of the coarse-grained crystal mush (Fig. 10c,d), as indicated by the intra-crystalline deformation and the very weak foliation in the coarse-grained olivine gabbros. Lack of well-developed Pl SPO and the occurrence of plastically deformed Ol, Pl and Cpx (Figs. 4, 5) in the weakly foliated coarse-grained olivine gabbros (Figs. 7, 9a) suggest that compaction was most efficient when crystals became interlocked and accommodated the strain (Fig. 10c). Mechanical interactions between grains result in an overall reduction in interstitial volume between crystals, that in turn led to expulsion of the interstitial melts. The chemical similarity between rims of coarse-grained crystals and unzoned fine-grained minerals indicate that a portion of that interstitial melt was retained in the coarse-grained intervals to crystallize the crystal rims, also further suggesting that compaction was relatively weak. In the melt-rich zones, where portions of extracted melts accumulated, the strain was taken up by the melt fraction and the undeformed fine-grained crystals were oriented preferentially along the direction of the melt flow, thus developing the observed weak foliations and lineations (Fig. 7, Fig. 8b, Fig. 9a, Fig. 10c). The lack of intra-

crystalline deformation indicates the fine-grained crystal matrix remained essentially undeformed during the entire crystallization history (see Section 6.2.1), in contrast with their coarse-grained counterpart.

Combined textural and geochemical constraints indicate that compaction of the crystal pile did not trigger upward melt migration through the coarse-grained crystal mush. Rather, compaction drove local melt extraction and accumulation in crystal-poor intervals, in turn generating local but ubiquitous grain-size variations in the olivine gabbros from the Atlantis Bank OCC.

7. Concluding remarks

At slow to ultraslow-spreading ridges, accretion is mainly accommodated by extensive faulting during discontinuous melt supply, a process that leads to strong crystal-plastic overprint on magmatic textures. Textures of primary magmatic processes are better preserved in the deepest portions of lower oceanic crustal sections observed at slow-spreading ridges. In IODP Hole U1473A at the Atlantis Bank OCC, olivine gabbros from the 500–800 mbsf depth interval preserve microstructural and chemical features of magmatic processes. Microstructural analyses, supported by the previous geochemical study of grain-size variations in these olivine gabbros, provide key evidence of melt migration and subsequent compaction-driven melt extraction in discrete intervals throughout the hole. The origin of heterogeneous grain-sizes in these olivine gabbros can be reconstructed as follows:

(i) Formation of the primitive crystal mush occurred beneath the SWIR axis. Cores of Ol, Pl and minor Cpx grew to form coarse-grained crystals. With more than 30% of melt present between the crystals, buoyancy-driven upward melt migration occurred through the mineral coarse-grained matrix;

(ii) Buoyancy-driven melt migration persisted as porosity and melt fraction decreased. Crystals began to interlock. Weak compaction led to very weak foliation and to deformation of the coarse-grained crystals under dislocation creep (Ol and Pl) and diffusion creep (mainly Pl) mechanisms. This resulted in the documented intra-crystalline deformation features (e.g., subgrain boundaries, bended pl around cpx, undulose extinction of cpx, high GOS and MGD);

(iii) Weak compaction of the coarse-grained crystal pile aided extraction of residual melts from the crystal mush into discrete 'melt-rich zones'. Here, local deformation was taken up by the melt fraction while fine-grained crystals remained undeformed; crystals oriented in the direction of melt transport, developing the observed weak lineation and foliations. High nucleation rates in these zones ultimately formed the fine-grained olivine gabbro.

We here provide an example of slow-spread oceanic crust where compaction is typically weak. Compaction is mainly recorded in the coarse-grained intervals and was identified by intra-crystalline deformation and very weak foliations without the occurrence of lineation. Weak foliations and lineations are instead observed in the fine-grained intervals where deformation likely occurred under coaxial strain with a component of non-coaxial strain. Processes of compaction can produce local, but ubiquitous, chemical and grain-size heterogeneities in a lower crustal section, as those observed in olivine gabbros from the Atlantis Bank OCC. Conversely, compaction had a minor role in the melt movement at larger scales (e.g., the whole crystal mush) within the oceanic crust, which occurred by porous flow, likely driven by positive buoyancy of the melt.

Supplementary data to this article can be found online at https://doi.org/10.1016/j.tecto.2021.229001.

Uncited references

CRediT authorship contribution statement

Declaration of Competing Interest

The authors declare that they have no known competing financial interests or personal relationships that could have appeared to influence the work reported in this paper.

Acknowledgments

References

Allard, M., Ildefonse, B., Oliot, E., 2020. Plastic deformation of plagioclase in a gabbro pluton at a slow-spreading ridge (IODP Hole U1473A, Atlantis Bank, Southwest Indian ridge). In: AGU Fall Meeting 2020, Abstract n°T026-0011.

Arai, S., Dick, H.J.B., Party, S., 2000. Cruise Report, Mode 2000 (Kairei/Kaiko KR00-06). Japanese Agency for Marine-Earth Science and Technology, Yokosuka, Japan.

Baines, A.G., Cheadle, M.J., Dick, H.J.B., Scheirer, A.H., John, B.E., Kusznir, N.J., Matsumoto, T., 2003. Mechanism for generating the anomalous uplift of oceanic core complexes: Atlantis Bank, Southwest Indian Ridge. Geology 31, 1105–1108. https://doi.org/10.1130/G19829.1.

Baines, G.A., Cheadle, M.J., Dick, H.J.B., Scheirer, A.H., John, B.E., Kusznir, N.J., Matsumoto, T., 2007. Evolution of the Southwest Indian ridge from 55°45′E to 62°E: changes in plate-boundary geometry since 26 Ma. Geochem. Geophys. Geosyst. 8. https://doi.org/10.1029/2006GC001559.

Baines, G.A., Cheadle, M.J., John, B.E., Schwartz, J.J., 2008. The rate of oceanic detachment faulting at Atlantis Bank, SW Indian Ridge. Earth Planet. Sci. Lett. 273, 105–114. https://doi.org/10.1016/j.epsl.2008.06.013.

Basch, V., Rampone, E., Crispini, L., Ferrando, C., Ildefonse, B., Godard, M., 2018. From mantle peridotites to hybrid troctolites: textural and chemical evolution during melt-rock interaction history. Lithos 323, 4–23. https://doi.org/10.1016/j.lithos.2018.02.025.

Basch, V., Rampone, E., Crispini, L., Ferrando, C., Ildefonse, B., Godard, M., 2019. Multi-stage reactive formation of troctolites in slow-spreading oceanic lithosphere (Erro – Tobbio, Italy): a combined field and petrochemical study. J. Petrol. 60, 873–906. https://doi.org/10.1093/petrology/egz019.

Bédard, J.H., 2015. Ophiolitic magma chamber process, a perspective from the Canadian Appalachians. In: Charlier, B., Namur, O., Latypov, R., Tegner, C. (Eds.), Layered Intrusions. Springer Geology. Springer, Dordrecht, pp. 693–732. https://doi.org/10.1007/978-94-017-9652-1_15.

Bertolett, E.M., Prior, D.J., Gravley, D.M., Hampton, S.J., Kennedy, B.M., 2019. Compacted cumulates revealed by electron backscatter diffraction analysis of plutonic lithics. Geology 47, 445–448. https://doi.org/10.1130/G45616.1.

Blackman, D.K., Ildefonse, B., John, B.E., Ohara, Y., Miller, D.J., Abe, N., Abratis, M., Andal, E.S., Andreani, M., Awaji, S., Beard, J.S., Brunelli, D., Charney, A.B., Christie, D.M., Collins, J., Delacour, A.G., Delius, H., Drouin, M., Einaudi, F., Escartín, J., Frost, B.R., Früh-Green, G., Fryer, P.B., Gee, J.S., Godard, M., Grimes, C.B., Halfpenny, A., Hansen, H.E., Harris, A.C., Tamura, A., Hayman, N.W., Hellebrand, E., Hirose, T., Hirth, J.G., Ishimaru, S., Johnson, K.T.M., Karner, G.D., Linek, M., MacLeod, C.J., Maeda, J., Mason, O.U., McCaig, A.M., Michibayashi, K., Morris, A., Nakagawa, T., Nozaka, T., Rosner, M., Searle, R.C., Suhr, G., Tominaga, M., von der Handt, A., Yamasaki, T., Zhao, X., 2011. Drilling constraints on lithospheric accretion and evolution at Atlantis Massif, Mid-Atlantic Ridge 30° N. J. Geophys. Res. 116, B07103. https://doi.org/10.1029/2010jb007931.

Boudier, F., Nicolas, A., Ildefonse, B., 1996. Magma chambers in the Oman ophiolite: fed from the top and the bottom. Earth Planet. Sci. Lett. 144, 239–250. https://doi.org/10.1016/0012-821X(96)00167-7.

Boulanger, M., France, L., Deans, J., Ferrando, C., Lissenberg, J., von der Handt, A., 2020. Magma reservoir formation and evolution at a slow-spreading center (Atlantis Bank, Southwest Indian Ridge). Front. Earth Sci. 8, 554598. https://doi.org/10.3389/feart.2020.554598.

Brothers, R.N., 1964. Petrofabric analyses of Rhum and Skaergaard layered rocks. J. Petrol. 5, 255–274. https://doi.org/10.1093/petrology/5.2.255.

Brown, T.C., Cheadle, M.J., John, B.E., Coogan, L.A., Gee, J.S., Karson, J.A., Swapp, S.M., 2019. Textural character of gabbroic rocks from Pito deep: a record of magmatic processes and the genesis of the upper plutonic crust at fast-spreading mid-ocean ridges. J. Petrol. 60, 997–1026. https://doi.org/10.1093/petrology/egz022.

Canales, J.P., Dunn, R.A., Arai, R., Sohn, R.A., 2017. Seismic imaging of magma sills beneath an ultramafic-hosted hydrothermal system. Geology 45, 451–454. https://doi.org/10.1130/G38795.1.

Cannat, M., Rommevaux-Jestin, C., Sauter, D., Deplus, C., Mendel, V., 1999. Formation of the axial relief at the very slow spreading Southwest Indian Ridge (49° to 69°E). J. Geophys. Res. 104843, 822–825. https://doi.org/10.1029/1999JB900195.

Cannat, M., Sauter, D., Mendel, V., Ruellan, E., Okino, K., Escartin, J., Combier, V., Baala, M., 2006. Modes of seafloor generation at a melt-poor ultraslow-spreading ridge. Geology 34, 605–608. https://doi.org/10.1130/G22486.1.

Cashman, K.V., Sparks, R.S.J., Blundy, J.D., 2017. Vertically extensive and unstable magmatic systems: A unified view of igneous processes. Science 355. https://doi.org/10.1126/science.aag3055.

Cheadle, M.J., Gee, J.S., 2017. Quantitative textural insights into the formation of gabbro in mafic intrusions. Elements 13, 409–414. https://doi.org/10.2138/gselements.13.6.409.

Coogan, L.A., Saunders, A.D., Kempton, P.D., Norry, M.J., 2000. Evidence from oceanic gabbros for porous melt migration within a crystal mush beneath the Mid-Atlantic Ridge. Geochem. Geophys. Geosyst. 1. https://doi.org/10.1029/2000GC000072.

Coogan, L.A., Jenkin, G.R.T., Wilson, R.N., 2007. Contrasting cooling rates in the lower oceanic crust at fast- and slow-spreading ridges revealed by geospeedometry. J. Petrol. 48, 2211–2231. https://doi.org/10.1093/petrology/egm057.

Detrick, R.S., Buhl, P., Vera, E., Mutter, J., Orcutt, J., Madsen, J., Brocher, T., 1987. Multi-channel seismic imaging of a crustal magma chamber along the East Pacific rise. Nature 326, 35–41. https://doi.org/10.1038/326035a0.

Dick, H.J.B., Meyer, P.S., Bloomer, S., Kirby, S., Stakes, D., Mawer, C., 1991a. Lithostratigraphic evolution of an in-situ section of oceanic Layer 3. In: Von Herzen, R.P., Robinson, P.T. (Eds.), et al., Proc. Ocean Drill. Program, Sci. Results, 118 Coll. Station. TX (Ocean Drill. Program). pp. 439–538. https://doi.org/10.2973/odp.proc.sr.118.128.1991.

Dick, H.J.B., Schouten, H., Meyer, P.S., Gallo, D.G., Bergh, H., Tyce, R., Patriat, P., Johnson, K.T.M., Snow, J., Fischer, A., 1991b. Tectonic evolution of the Atlantis II Fracture Zone. In: Von Herzen, R.P., Robinson, P.T. (Eds.), et al., Proc. Ocean Drill. Program, Sci. Results, 118 Coll. Station. TX (Ocean Drill. Program). pp. 359–398.

Dick, H.J.B., Natland, J.H., Alt, J.C., Bach, W., Bideau, D., Gee, J.S., Haggas, S., Hertogen, J.G.H., Hirth, G., Holm, P.M., Ildefonse, B., Iturrino, G.J., John, B.E., Kelley, D.S., Kikawa, E., Kingdon, A., LeRoux, P.J., Maeda, J., Meyer, P.S., Miller, D.J., Naslund, H.R., Niu, Y.-L., Robinson, P.T., Snow, J., Stephen, R.A., Trimby, P.W., Worm, H.-U., Yoshinobu, A., 2000. A long in situ section of the lower ocean crust: results of ODP Leg 176 drilling at the Southwest Indian Ridge. Earth Planet. Sci. Lett. 179, 31–51. https://doi.org/10.1016/S0012-821X(00)00102-3.

Dick, H.J.B., Ozawa, K., Meyer, P.S., Niu, Y., Robinson, P.T., Constantin, M., Hebert, R., Maeda, J., Natland, J.H., Hirth, J.G., Mackie, S.M., 2002. Primary silicate mineral chemistry of a 1.5-km section of very slow spreading lower ocean crust: ODP Hole 735B, Southwest Indian Ridge. In: Natland, J.H., Dick, H.J.B., Miller, D.J., Von Herzen, R.P. (Eds.), Ocean Drill. Program, Sci. Results, 176 Coll. Station. TX (Ocean Drill. Program). pp. 1–61. https://doi.org/10.2973/odp.proc.sr.176.001.2002.

Dick, H.J.B., Kvassnes, A.J.S., Robinson, P.T., MacLeod, C.J., Kinoshita, H., 2019a. The Atlantis Bank Gabbro Massif, Southwest Indian Ridge. Prog. Earth Planet. Sci. 6, 64. https://doi.org/10.1186/s40645-019-0307-9.

Dick, H.J.B., Macleod, C.J., Blum, P., Abe, N., Blackman, D.K., Bowles, J.A., Cheadle, M.J., Cho, K., Ciążela, J., Deans, J.R., Edgcomb, V.P., Ferrando, C., France, L., Ghosh, B., Ildefonse, B., John, B., Kendrick, M.A., Koepke, J., Leong, J.A.M., Liu, C., Ma, Q., Morishita, T., Morris, A., Natland, J.H., Nozaka, T., Pluemper, O., Sanfilippo, A., Sylvan, J.B., Tivey, M.A., Tribuzio, R., Viegas, G., 2019b. Dynamic accretion beneath a slow-spreading ridge segment: IODP Hole 1473A and the Atlantis Bank Oceanic Core complex. J. Geophys. Res. Solid Earth 124, 2631–12659. https://doi.org/10.1029/2018JB016858.

Dimanov, A., Dresen, G., 2005. Rheology of synthetic anorthite-diopside aggregates: implications for ductile shear zones. J. Geophys. Res. 110. https://doi.org/10.1029/2004JB003431.

Dimanov, A., Dresen, G., Wirth, R., 1998. High-temperature creep of partially molten plagioclase aggregates. J. Geophys. Res. 103, 9651–9664. https://doi.org/10.1029/97JB03742.

Escartín, J., Smith, D.K., Cann, J., Schouten, H., Langmuir, C.H., Escrig, S., 2008. Central role of detachment faults in accretion of slow-spreading oceanic lithosphere. Nature 455, 790–794. https://doi.org/10.1038/nature07333.

Feig, S.T., Koepke, J., Snow, J.E., 2006. Effect of water on tholeiitic basalt phase equilibria: an experimental study under oxidizing conditions. Contrib. Mineral. Petrol. 152, 611–638. https://doi.org/10.1007/s00410-006-0123-2.

Ferrando, C., Godard, M., Ildefonse, B., Rampone, E., 2018. Melt transport and mantle

assimilation at Atlantis Massif (IODP Site U1309): Constraints from geochemical modeling. Lithos 323, 24–43. https://doi.org/10.1016/j.lithos.2018.01.012.

Ferrando, C., Lynn, K.J., Basch, V., Ildefonse, B., Godard, M., 2020. Retrieving timescales of oceanic crustal evolution at Oceanic Core Complexes: Insights from diffusion modelling of geochemical profiles in olivine. Lithos 376–377, 105727. https://doi.org/10.1016/j.lithos.2020.105727.

Ferrando, C., France, L., Basch, V., Sanfilippo, A., Tribuzio, R., Boulanger, M., 2021. Grain size variations record segregation of residual melts in slow-spreading oceanic crust (Atlantis Bank, 57°E Southwest Indian Ridge). J. Geophys. Res. Solid Earth 126, e2020JB020997. https://doi.org/10.1029/2020JB020997.

France, L., Ildefonse, B., Koepke, J., 2009. Interactions between magma and hydrothermal system in Oman ophiolite and in IODP Hole 1256D: fossilization of a dynamic melt lens at fast spreading ridges. Geochem. Geophys. Geosyst. 10–10, Q10O19. https://doi.org/10.1029/2009GC002652.

France, L., Lombard, M., Nicollet, C., Berthod, C., Debret, B., Koepke, J., Ildefonse, B., Toussaint, A., 2021. Quantifying the axial magma lens dynamics at the roof of oceanic magma reservoirs (dike/gabbro transition): oman drilling project GT3 site survey. J. Geophys. Res. Solid Earth 126, e2020JB021496. https://doi.org/10.1029/2020JB021496.

Gao, Y., Hoefs, J., Hellebrand, E., von der Handt, A., Snow, J.E., 2007. Trace element zoning in pyroxenes from ODP Hole 735B gabbros: diffusive exchange or synkinematic crystal fractionation?. Contrib. Mineral. Petrol. 153, 429–442. https://doi.org/10.1007/s00410-006-0158-4.

Hess, H.H., 1960. Stillwater igneous complex, Montana: a quantitative mineralogical study. Geol. Soc. Am. Mem. 80, 230. https://doi.org/10.1130/MEM80.

Higgins, M.D., 1991. The origin of laminated and massive anorthosite, Sept Iles layered intrusion, Quebec. Canada. Contrib. Mineral. Petrol. 106, 340–354. https://doi.org/10.1007/BF00324562.

Higgins, M.D., 2006. Quantitative Textural Measurements in Igneous and Metamorphic Petrology. Cambridge University Press, Cambridge, p. 265. https://doi.org/10.1017/CBO9780511535574.

Holness, M.B., Vukmanovic, Z., Mariani, E., 2017. Assessing the role of compaction in the formation of adcumulates: a microstructural perspective. J. Petrol. 58, 643–674. https://doi.org/10.1093/petrology/egx037.

Hosford, A., Tivey, M., Matsumoto, T., Dick, H., Schouten, H., Kinoshita, H., 2003. Crustal magnetization and accretion at the Southwest Indian Ridge near the Atlantis II fracture zone, 0–25 Ma. J. Geophys. Res. Solid Earth 108, 1–23. https://doi.org/10.1029/2001JB000604.

Ildefonse, B., Sokoutis, D., Mancktelow, N.S., 1992. Mechanical interactions between rigid particles in a deforming ductile matrix. Analogue experiments in simple shear flow. J. Struct. Geol. 14, 1253–1266. https://doi.org/10.1016/0191-8141(92)90074-7.

Ildefonse, B., Arbaret, L., Diot, H., 1997. Rigid particles in simple shear flow: is their preferred orientation periodic or steady-state?. In: Bouchez, J.L. (Ed.), et al., Granite: From Segregation of Melt to Emplacement Fabrics. Kluwer Academic Publishers, pp. 177–185.

Ildefonse, B., Blackman, D.K., John, B.E., Ohara, Y., Miller, D.J., MacLeod, C.J., Abe, N., Abratis, M., Andal, E.S., Andréani, M., Awaji, S., Beard, J.S., Brunelli, D., Charney, A.B., Christie, D.M., Delacour, A.G., Delius, H., Drouin, M., Einaudi, F., Escartin, J., Frost, B. R., Fryer, P.B., Gee, J.S., Godard, M., Grimes, C.B., Halfpenny, A., Hansen, H.E., Harris, A.C., Hayman, N.W., Hellebrand, E., Hirose, T., Hirth, J.G., Ishimaru, S., Johnson, K.T. M., Karner, G.D., Linek, M., Maeda, J., Mason, O.U., McCaig, A.M., Michibayashi, K., Morris, A., Nakagawa, T., Nozaka, T., Rosner, M., Searle, R.C., Suhr, G., Tamura, A., Tominaga, M., von der Handt, A., Yamasaki, T., Zhao, X., 2007. Oceanic core complexes and crustal accretion at slow-spreading ridges. Geology 35, 623–626. https://doi.org/10.1130/G23531A.1.

Ji, S., Shao, T., Salisbury, M.H., Sun, S., Michibayashi, K., Zhao, W., Long, C., Liang, F., Satsukawa, T., 2014. Plagioclase preferred orientation and induced seismic anisotropy in mafic igneous rocks. J. Geophys. Res. Solid Earth 119, 8064–8088. https://doi.org/10.1002/2014JB011352.

John, B.E., Foster, D.A., Murphy, J.M., Cheadle, M.J., Baines, A.G., Fanning, C.M., Copeland, P., 2004. Determining the cooling history of in situ lower oceanic crust-Atlantis Bank, SW Indian Ridge. Earth Planet. Sci. Lett. 222, 145–160. https://doi.org/10.1016/j.epsl.2004.02.014.

Kelemen, P.B., Aharonov, E., 1998. Periodic formation of magma fractures and generation of layered gabbros in the lower crust beneath oceanic spreading ridges. In: Buck, W.R., Delaney, P.T., Karson, J.A., Lagabrielle, Y. (Eds.), Faulting and Magmatism at Mid-Ocean Ridges. Geophys. Monogr. Ser., 106. American Geophysical Union, pp. 267–289. https://doi.org/10.1029/GM106p0267.

Lamoureux, G., Ildefonse, B., Mainprice, D., 1999. Modelling the seismic properties of fast-spreading ridge crustal Low-Velocity zones: insights from Oman gabbro textures. Tectonophysics 312, 283–301. https://doi.org/10.1016/s0040-1951(99)00183-3.

Leuthold, J., Blundy, J.D., Holness, M.B., Sides, R., 2014. Successive episodes of reactive liquid flow through a layered intrusion (Unit 9, Rum Eastern Layered Intrusion, Scotland). Contrib. Mineral. Petrol. Mineral. Petrol. 168, 1021. https://doi.org/10.1007/s00410-014-1021-7.

Lissenberg, C.J., Dick, H.J.B., 2008. Melt-rock reaction in the lower oceanic crust and its implications for the genesis of mid-ocean ridge basalt. Earth Planet. Sci. Lett. 271, 311–325. https://doi.org/10.1016/j.epsl.2008.04.023.

Lissenberg, C.J., MacLeod, C.J., 2016. A reactive porous flow control on mid-ocean ridge magmatic evolution. J. Petrol. 57, 2195–2220. https://doi.org/10.1093/petrology/egw074.

Lissenberg, C.J., MacLeod, C.J., Howard, K.A., Godard, M., 2013. Pervasive reactive melt migration through fast-spreading lower oceanic crust (Hess deep, equatorial Pacific Ocean). Earth Planet. Sci. Lett. 361, 436–447. https://doi.org/10.1016/j.epsl.2012.11.012.

Lissenberg, C.J., MacLeod, C.J., Bennett, E.N., 2019. Consequences of a crystal mush-

dominated magma plumbing system: a mid-ocean ridge perspective. Philos. Trans. R. Soc. A 377, 20180. https://doi.org/10.1098/rsta.2018.0014.

MacLeod, C.J., Boudier, F., Yaouancq, G., Richter, C., 1996. Gabbro fabrics from Site 894, Hess deep: implications for magma chamber processes at the East Pacific rise. Proc. Ocean Drill. Program Sci. Results 147, 317–328.

MacLeod, C.J., Dick, H.J.B., Allerton, S., Robinson, P.T., Coogan, L.A., Edwards, S.J., Galley, A., Gillis, K.M., Hirth, G., Hunter, A.G., Hutchinson, D., Kvassnes, A.J., Natland, J.H., Salisbury, M., Schandl, E.S., Stakes, D.S., Thompson, G.M., Tivey, M.A., 1998. Geological mapping of slow-spread lower ocean crust: a deep-towed video and wireline rock drilling survey of Atlantis Bank (ODP Site 735, SW Indian Ridge). InterRidge News 7 (2), 39–43.

MacLeod, C.J., Searle, R.C., Murton, B.J., Casey, J.F., Mallows, C., Unsworth, S.C., Achenbach, K.L., Harris, M., 2009. Life cycle of oceanic core complexes. Earth Planet. Sci. Lett. 287, 333–344. https://doi.org/10.1016/j.epsl.2009.08.016.

MacLeod, C.J., Dick, H.J.B., Blum, P., Abe, N., Blackman, D.K., Bowles, J.A., Cheadle, M. J., Cho, K., Ciazela, J., Deans, J.R., Edgcomb, V.P., Ferrando, C., France, L., Ghosh, B., Ildefonse, B.M., Kendrick, M.A., Koepke, J.H., Leong, J.A.M., Liu, C., Ma, Q., Morishita, T., Morris, A., Natland, J.H., Nozaka, T., Pluemper, O., Sanfilippo, A., Sylvan, J.B., Tivey, M.A., Tribuzio, R., Viegas, L.G.F., 2017. IODP expedition 360. Proc. Int. Ocean Discov. Progr. 360, 1–51. https://doi.org/10.14379/iodp.proc.360.101.2017.

Mainprice, D., Bachmann, F., Hielscher, R., Schaeben, H., 2014. Descriptive tools for the analysis of texture projects with large datasets using MTEX: strength, symmetry and components. In: Faulkner, D.R., Mariani, E., Mecklenburgh, J. (Eds.), Rock deformation from field, experiments and theory: a volume in honour of Ernie Rutter, 409. Geological Society, London, Spec. Pub. https://doi.org/10.1144/SP409.8.

Matsumoto, T., Dick, H.J.B., Cruise, A., 2002. In-situ Observation of the Lower Crust and Upper Mantle Lithology in Atlantis Bank, SWIR - Results from ABCDE Cruise, EOS, Transactions of the American Geophysical Union. p. 83.

McKenzie, D.P., 1984. The generation and compaction of partial melts. J. Pet. 25, 713–765.

Means, W.D., Park, Y., 1994. New experimental approach to understanding igneous texture. Geology 22, 323–326.

Meurer, W.P., Boudreau, A.E., 1998. Compaction of igneous cumulates part II: compaction and the development of igneous foliations. J. Geol. 106, 293–304. https://doi.org/10.1086/516023.

Meyer, P.S., Dick, H.J.B., Thompson, G., 1989. Cumulate gabbros from the Southwest Indian Ridge, 54°S-7°16′E: Implications for magmatic processes at a slow spreading ridge. Contrib. Mineral. Petrol. 103, 44–63. https://doi.org/10.1007/BF00371364.

Minshull, T.A., Muller, M.R., Robinson, C.J., White, R.S., Bickle, M.J., 1998. Is the oceanic Moho a serpentinization front?. In: Mills, R.A., Harrison, K. (Eds.), Modern Ocean Floor Processes and the Geological Record. In: Geological Society Spec. Pub., 148(1) 148(1). pp. 71–80. https://doi.org/10.1144/GSL.SP.1998.148.01.05.

Miranda, E.A., John, B.E., 2010. Strain localization along the Atlantis Bank oceanic detachment fault system, Southwest Indian Ridge. Geochem. Geophys. Geosyst. 11. https://doi.org/10.1029/2009GC002646.

Morales, L.F.G., Boudier, F., Nicolas, A., 2011. Microstructures and crystallographic preferred orientation of anorthosites from Oman ophiolite and the dynamics of melt lenses. Tectonics 30. https://doi.org/10.1029/2010TC002697.

Morgan, J.P., Chen, Y.J., 1993. The genesis of oceanic crust: Magma injection, hydrothermal circulation, and crustal flow. J. Geophys. Res. Solid Earth 98, 6283–6297. https://doi.org/10.1029/92JB02650.

Muller, M.R., Minshull, T.A., White, R.S., 1999. Segmentation and melt supply at the Southwest Indian Ridge. Geology 27, 867–870. https://doi.org/10.1130/0091-7613(1999)027<0867:SAMSAT>2.3.CO;2.

Namur, O., Abily, B., Boudreau, A.E., Blanchette, F., 2015. Igneous layering in basaltic magma chambers. In: Charlier, B., Namur, O., Latypov, R., Tegner, C. (Eds.), Layered Intrusions. Springer Geology. https://doi.org/10.1007/978-94-017-9652-1.

Natland, J.H., Dick, H.J.B., 2001. Formation of the lower ocean crust and the crystallization of gabbroic cumulates at a very slowly spreading ridge. J. Volcanol. Geotherm. Res. 110, 191–233. https://doi.org/10.1016/S0377-0273(01)00211-6.

Natland, J.H., Dick, H.J.B., 2002. Stratigraphy and composition of gabbros drilled in ODP Hole 735B, SW Indian Ocean: a synthesis of geochemical data. In: Natland, J.H., Dick, H. J.B., Miller, D.J., Von Herzen, R.P. (Eds.), Proc. Ocean Dril. Prog., Scientific Results. Ocean Drilling Program, College Station, TX. https://doi.org/10.2973/odp.proc.sr.176.021.2002.

Nicolas, A., 1992. Kinematics in magmatic rocks with special reference to gabbros. J. Petrol. 33, 891–915. https://doi.org/10.1093/petrology/33.4.891.

Nicolas, A., Ildefonse, B., 1996. Flow mechanism and viscosity in basaltic magma chambers. Geophys. Res. Lett. 23, 2013–2016. https://doi.org/10.1029/96GL02073.

Nicolas, A., Ceuleneer, G., Boudier, F., Misseri, M., 1988. Structural mapping in the Oman ophiolites: Mantle diapirism along an oceanic ridge. In: Boudier, F., Nicolas, A. (Eds.), The Ophiolites of Oman. In: Tectonophysics, 151. pp. 27–55. https://doi.org/10.1016/0040-1951(88)90239-9.

Nicolas, A., Boudier, F., France, L., 2009. Subsidence in magma chamber and the development of magmatic foliation in Oman ophiolite gabbros. Earth Planet. Sci. Lett. 284, 76–87. https://doi.org/10.1016/j.epsl.2009.04.012.

Palmiotto, C., Corda, L., Ligi, M., Cipriani, A., Dick, H.J.B., Douville, E., Gasperini, L., Montagna, P., Thil, F., Borsetti, A.M., Balestra, B., Bonatti, E., 2013. Nonvolcanic tectonic islands in ancient and modern oceans. Geochem. Geophys. Geosyst. 14, 10. https://doi.org/10.1002/ggge.20279.

Park, Y., Means, W.D., 1996. Direct observation of deformation processes in crystal mushes. J. Struct. Geol. 18, 847–858. https://doi.org/10.1016/S0191-8141(96)80017-4.

Park, Y., Means, W.D., 1997. Crystal rotation and growth during grain flow in a deforming crystal mush. In: Sengupta, S. (Ed.), Evolution of Geological Structures in Micro- to Macro-Scales. Springer, Dordrecht. https://doi.org/10.1007/978-94-011-5870-1_15.

Pettigrew, T.L., Casey, J.F., Miller, D.J., et al., 1999. Proceedings of the Ocean Drilling Program, Initial Reports. 179. Ocean Drilling Program, College Station, TX. https://doi.org/10.2973/odp.proc.ir.179.1999.

Quick, J.E., Denlinger, R.P., 1993. Ductile deformation and the origin of layered gabbro in ophiolites. J. Geophys. Res. 98, 14015–14027. https://doi.org/10.1029/93JB00698.

Rampone, E., Borghini, G., Basch, V., 2020. Melt migration and melt-rock reaction in the Alpine-Apennine peridotites: insights on mantle dynamics in extending lithosphere. Geosci. Front. 11, 151–166. https://doi.org/10.1016/j.gsf.2018.11.001.

Rioux, M., Cheadle, M.J., John, B.E., Bowring, S.A., 2016. The temporal and spatial distribution of magmatism during lower crustal accretion at an ultraslow-spreading ridge: High-precision U–Pb zircon dating of ODP Holes 735B and 1105A, Atlantis Bank, Southwest Indian Ridge. Earth Planet. Sci. Lett. 449, 395–406. https://doi.org/10.1016/j.epsl.2016.05.047.

Rybacki, E., Dresen, G., 2000. Dislocation and diffusion creep of synthetic anorthite aggregates. J. Geophys. Res. 105, 26017–26036. https://doi.org/10.1029/2000JB900223.

Sanfilippo, A., Tribuzio, R., Tiepolo, M., Berno, D., 2015. Reactive flow as dominant evolution process in the lowermost oceanic crust: evidence from olivine of the Pineto ophiolite (Corsica). Contrib. Mineral. Petrol. 170. https://doi.org/10.1007/s00410-015-1194-8.

Sanfilippo, A., MacLeod, C.J., Tribuzio, R., Lissenberg, C.J., Zanetti, A., 2020. Early-stage melt-rock reaction in a cooling crystal mush beneath a slow-spreading mid-ocean ridge (IODP Hole U1473A, Atlantis Bank, Southwest Indian Ridge). Front. Earth Sci. 8, 473. https://doi.org/10.3389/feart.2020.579138.

Satsukawa, T., Ildefonse, B., Mainprice, D., Morales, L.F.G., Michibayashi, K., Barou, F., 2013. A database of plagioclase crystal preferred orientations (CPO) and microstructures-implications for CPO origin, strength, symmetry and seismic anisotropy in gabbroic rocks. Solid Earth 4, 511–542. https://doi.org/10.5194/se-4-511-2013.

Schoolmeesters, N., Cheadle, M.J., John, B.E., Reiners, P.W., Gee, J., Grimes, C.B., 2012. The cooling history and the depth of detachment faulting at the Atlantis Massif oceanic core complex. Geochem. Geophys. Geosyst. 13, 1–19. https://doi.org/10.1029/2012GC004314.

Sinton, J.M., Detrick, R.S., 1992. Mid-ocean ridge magma chambers. J. Geophys. Res. 97, 197–216. https://doi.org/10.1029/91JB02508.

Van der Molen, I., Paterson, M.S., 1979. Experimental deformation of partially-melted granite. Contrib. Mineral. Petrol. 70, 299–318. https://doi.org/10.1007/BF00375359.

VanTongeren, J.A., Hirth, G., Kelemen, P.B., 2015. Constraints on the accretion of the gabbroic lower oceanic crust from plagioclase lattice preferred orientation in the Samail ophiolite. Earth Planet. Sci. Lett. 427, 249–261. https://doi.org/10.1016/j.epsl.2015.07.001.

Vukmanovic, Z., Holness, M.B., Monks, K., Andersen, J.C.Ø., 2018. The Skaergaard trough layering: sedimentation in a convecting magma chamber. Contrib. Mineral. Petrol. 173, 43. https://doi.org/10.1007/s00410-018-1466-1.

Wager, L.R., Brown, G.M., 1968. Layered Igneous Rocks. Oliver and Boyd, Edinburgh.

Woodcock, N.H., 1977. Specification of fabric shapes using an eigenvalue method. Geol. Soc. Am. Bull. 88, 1231–1236. https://doi.org/10.1130/0016-7606(1977)88<1231:SOFSUA>2.0.CO;2.

Yaouancq, G., Macleod, C.J., 2000. Petrofabric investigation of gabbros from the Oman Ophiolite: comparison between AMS and rock fabric. Mar. Geophys. Res. 21, 289–305. https://doi.org/10.1023/A:1026774111021.

Yu, X., Dick, H.J.B., 2020. Plate-driven micro-hotspots and the evolution of the Dragon Flag melting anomaly, Southwest Indian Ridge. Earth Planet. Sci. Lett. 531, 116002. https://doi.org/10.1016/j.epsl.2019.116002.

Zhang, W.-Q., Liu, C.-Z., Dick, H.J.B., 2020. Evidence for multi-stage melt transport in the lower ocean crust: the Atlantis Bank Gabbroic Massif (IODP Hole U1473A, SW Indian Ridge). J. Petrol. 61, egaa082. https://doi.org/10.1093/petrology/egaa082.

Zhang, W.-Q., Dick, H.J.B., Liu, C.-Z., Lin, Y.-Z., Angeloni, L.M., 2021. MORB melt transport through Atlantis Bank oceanic batholith (SW Indian Ridge). J. Petrol. egab034. https://doi.org/10.1093/petrology/egab034.